Automated model discovery for textile structures: The unique mechanical signature of warp knitted fabrics

Jeremy A. McCulloch, Ellen Kuhl

Department of Mechanical Engineering, Stanford University, Stanford, California, United States

Abstract

Textile fabrics have unique mechanical properties, which make them ideal candidates for many engineering and medical applications: They are initially flexible, nonlinearly stiffening, and ultra-anisotropic. Various studies have characterized the response of textile structures to mechanical loading; yet, our understanding of their exceptional properties and functions remains incomplete. Here we integrate biaxial testing and constitutive neural networks to automatically discover the best model and parameters to characterize warp knitted polypropylene fabrics. We use experiments from different mounting orientations, and discover interpretable anisotropic models that perform well during both training and testing. Our study shows that constitutive models for warp knitted fabrics are highly sensitive to an accurate representation of the textile microstructure, and that models with three microstructural directions outperform classical orthotropic models with only two in-plane directions. Strikingly, out of 2^{14} =16,384 possible combinations of terms, we consistently discover models with two exponential linear fourth invariant terms that inherently capture the initial flexibility of the virgin mesh and the pronounced nonlinear stiffening as the loops of the mesh tighten. We anticipate that the tools we have developed and prototyped here will generalize naturally to other textile fabrics–woven or knitted, weft knit or warp knit, polymeric or metallic–and, ultimately, will enable the robust discovery of anisotropic constitutive models for a wide variety of textile structures. Beyond discovering constitutive models, we envision to exploit automated model discovery as a novel strategy for the generative material design of wearable devices, stretchable electronics, and smart fabrics, as programmable textile metamaterials with tunable properties and functions. Our source code, data, and examples are available at https://github.com/LivingMatterLab/CANN.

Keywords: textile structures; knitted fabrics; biaxial testing; constitutive modeling; anisotropy; constitutive neural networks; machine learning

1. Motivation

Synthetic meshes have unique mechanical properties [1], which make them ideal candidates for many engineering and medical applications [14]: Under small deformations they display a remarkable *initial flexibility*, under large deformations, they exhibit a pronounced *nonlinear stiffening*, and under varying loading scenarios, they reveal an *ultra-anisotropic response* [13]. Their compliant nature allows them to effortlessly undergo large deformations while maintaining structural integrity [6]. Their inherent porosity encourages fluid flow and nutrient exchange, crucial for many biological or technical functions [32]. Their anisotropic nature enables them to adapt and function effectively in complex dynamic environments [31]. Collectively, these unique features make meshes highly suitable for a range of biomedical applications, including surgical repair, drug delivery, wound healing, implant design, and tissue engineering [30]. Beyond biomedicine, meshes are becoming increasingly popular in other technical applications including filtration systems, protective gear, flexible electronics, and structural reinforcement [22].

The microstructure of the mesh is critical to its function. The mechanical properties of the mesh directly affect how well it integrates within its environment, distributes stresses, and provides structural support [4]. In fabric mechanics, we distinguish two fundamentally different types of meshes: woven and knitted [13]. The microstructure of *woven* fabrics consists of warp threads running lengthwise and shute or weft threads

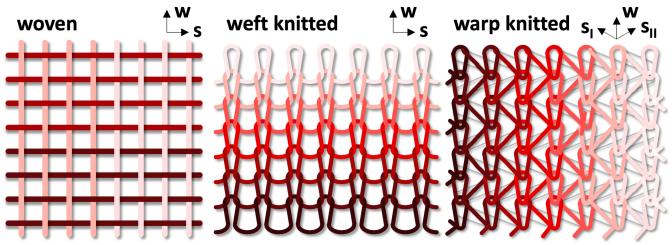

Figure 1: **Microstructure of woven, weft and warp knitted fabrics.** Woven fabrics consist of a series of parallel warp strands alternately passed over and under by a set of parallel shute strands creating a microstructure with two orthogonal directions, the warp direction $\boldsymbol{w}$ and the shute direction $\boldsymbol{s}$. Knitted fabrics consists of continuous filaments that are looped around one another. Weft knitted fabrics consists of horizontal rows of interlocking loops creating a microstructure with two orthogonal directions, the production or wale direction $\boldsymbol{w}$ and the yarn direction $\boldsymbol{s}$. Warp knitted fabrics consists of vertical columns of interlocking loops creating a microstructure with a warp direction $\boldsymbol{w}$ and one or more yarn directions $\boldsymbol{s}_I$ and $\boldsymbol{s}_{II}$.

running widthwise. The shute threads are woven over and under the warp threads interlacing them at right angles to create a tight and stable grid-like pattern with two orthogonal microstructural directions, the warp direction $\boldsymbol{w}$ and the shute direction $\boldsymbol{s}$. Along these directions, woven fabrics are rather stiff; off-set at 45 degrees, they are fairly compliant, meaning they have a high tensile stiffness, but a low shear stiffness [34]. The microstructure of *knitted* fabrics consists of interlocking loops of yarn, creating a flexible and stretchable textile structure that can easily adapt its shape and undergo large deformations while maintaining structural integrity [17]. We distinguish two families of knitted structures: weft-knitted and warp knitted [15]. The microstructure of *weft knitted* fabrics consists of horizontal rows of interlocking loops. It is made by looping a single yarn back and forth horizontally across the fabric width, creating interconnected loops, row by row, with two orthogonal microstructural directions, the production or wale direction $\boldsymbol{w}$ and the yarn direction $\boldsymbol{s}$. Regardless of the direction of loading, weft knitted fabrics tend to be extremely extensible and dimensionally unstable [43]. The microstructure of *warp knitted* fabrics consists of vertical columns of interlocking loops. It is made by looping multiple parallel yarns vertically along the fabric length, zigzagging between two neighboring columns, creating interconnected loops, column by column, with the production or warp direction $\boldsymbol{w}$ and one or multiple yarn directions $\boldsymbol{s}_I$ and $\boldsymbol{s}_{II}$. In the warp direction, warp-knitted fabrics are fairly stiff; in the yarn directions, the stiffness is tunable by the interlocking pattern [39]. Of the three different microstructures in Figure 1, warp knitted structures are the most tunable: The design space of a single loop spans $3 \times 2 \times 3 = 18$ possibile configurations, three for the incoming yarn, two for the loop itself–open or closed–, and three for the outgoing yarn [15]. For warp knitted structures made with two guide bars, this already results in $18 \times 18 = 324$ possible combinations, and modern knitting machines have four or more guide bars. This opens tremendous opportunities to design warp knitted fabrics with mechanically-guided microstructures and custom-designed properties [2].

Synthetic meshes play an integral role in surgical repair. Initially introduced for hernia repair in the 1950s, the primary goal of synthetic meshes is to reinforce weakened or damaged structures and provide durable structural integrity. Hernia repair is a common surgery, with more than 20 million procedures each year [42]. In spite of this high prevalence, complications are relatively common, with 11 percent of patients reporting postoperative abdominal pain [33]. Hernia repairs use various methods to close the wound in the abdominal wall, but the most common surgical intervention is to suture a synthetic mesh over the wound [50]. It is essential that the surgeon selects a mesh with appropriate mechanical properties, as a mismatch between the mechanics of the mesh and the surrounding tissue can increase the risk of postoperative failure [4]. To assess the mechanical biocompatibility of a synthetic mesh, we must understand its mechanical properties [9]. Thus, there is a critical need to develop constitutive models for synthetic meshes to better understand how they interact with the surrounding tissue [24]. Previous studies have performed biaxial testing of various mesh patches [6]; however, these studies only extracted a few phenomenological parameters and did not combine data from multiple experiments into a unified mechanistic constitutive model. The benefit of obtaining a fully three-dimensional hyperelastic constitutive model from experimental data is that such a model would describe the stress state of the mesh induced by *any* possible deformation, including complex states that we do not test experimentally, but may well occur in vivo [40]. However, here we will *not* follow the traditional approach, propose yet another phenomenological model, and fit its parameters to data. Instead, *our objective is to discover a microstructurally motivated hyperelastic constitutive model for warp-knitted fabrics and establish a robust set of experimental and computational techniques to autonomously discover the best constitutive models and parameters for a variety of woven, weft and warp knitted textile structures and other synthetic microstructural materials.*

Constitutive modeling requires deep expert knowledge. A constitutive model aims to predict the internal stress state of a material as a function of its strain. In particular, in developing elastic constitutive models, we assume that the Piola stress tensor is a function of the deformation gradient tensor [12]. There are various approaches to infer this relationship between the deformation gradient and the Piola stress from mechanical testing data. Classical approaches attempt to fit a few unknown parameters of well-known phenomenological models such as the neo Hooke model [48], the Lanir model [16], or the Demiray model [5]. The challenge with this approach is that it requires a profound domain expertise to select an appropriate model, and we may need to repeat model selection and parameter identification several times to identify a model that fits the data well. Constitutive neural networks use physics-informed insights about constitutive models as well as powerful deep learning methods to simultaneously discover the function form of the constitutive model and learn its appropriate parameters [19]. While the first family of constitutive neural networks only discovered isotropic models for materials such as rubber [19], brain [20] or plant-based meat [37], more recent networks can now discover transversely isotropic models for skin [21] or arteries [35]. Here we explore how to expand constitutive neural networks to discover more complex anistropic constitutive models from biaxial extension data.

Constitutive neural networks can autonomously discover the best model and parameters. A constitutive neural network is a machine learning model that takes the deformation gradient as an input and outputs the Piola stress for a specific material [18]. Constitutitve artificial neural networks take advantage of physical laws and assumptions about the material to constrain the input-output relationship that the network discovers, similar to physics-informed neural networks [38]. However, constitutive neural networks differ from physics-informed neural networks, which alter the loss function to satisfy physical laws. Instead, constitutive neural networks modify the architecture of the underlying machine learning model such that, regardless of the model parameters, the discovered model exactly satisfies the relevant physical laws [19]. The particular as-

sumptions that motivate the design of hyperelastic constitutive neural networks are material objectivity, thermodynamic consistency, incompressibility, and material symmetry. Prior work has enforced various forms of symmetry including isotropy [19], transverse isotropy [21], and orthotropy [23]; here we assume that warp-knitted meshes have either two or three characteristic microstructural orientations in the plane of the mesh. Unlike most previous work that trains anisotropic constitutive neural networks exclusively by using homogeneous tests [46], we explore how to use biaxial testing data when neither of the loading axes are aligned with the symmetry planes of the material [41]. We acknowledge that this violates the condition of homogeneity; yet, it allows us to train our network with a broader class of deformations, and discover models that are more robust when predicting stresses in response to deformation states that the network has not previously seen during training [47]. Finally, while constitutive neural networks are able to discover constitutive models by selecting from a large set of possible strain energy functions, the most useful constitutive models have only a small number of parameters and are therefore interpretable [3]. Various regularization techniques can help reduce the number of non-zero parameters without significantly sacrificing model accuracy [10]. Prior work has shown that, when computationally tractable, L_0 regularization is the best method for identifying the optimal n-term model for a fixed, small n [25]. When n is too large for L_0 optimization, L_p regularization with $0 < p \leq 1$ can effectively reduce the number of non-zero terms [36], without significantly decreasing model accuracy [8]. Here we will apply both approaches, compare the discovered models, and make recommendations which regularization to choose.

2. Methods

2.1. Experimental methods

We prepared samples from a 0.5 mm thick warp knitted surgical mesh of extruded polypropylene designed for surgical repair (PROLENE® Ethicon, Inc., Somerville, NJ), to test under biaxial loading in a CellScale BioTester 5000. We define the *warp direction* of the mesh as the direction along which the loops are aligned, which is also the direction in which the mesh is stiffest. We then define the *shute directions* in the plane of the mesh, either as one direction orthogonal to the warp direction inclined by 90 degrees, or as two directions symmetrically inclined to the warp direction by 60 degrees. We cut the mesh into square sections two different orientations: In the first orientation, which we denote as the *0/90 orientation* or *0/+60/-60 orientation*, the sample is aligned with the warp direction; in the second orientation, which we denote as the *-45/+45 orientation* or *-45/+15/+75 orientation*, the sides of the sample are 45 degrees offset from the warp direction. Figure 2 illustrates the samples of each orientation, mounted into the testing device. In the 0/90 or 0/+60/-60 orientation, in the left column, we place the tines of the biaxial testing device in the loops of the mesh. To prevent the mesh from unravelling, we avoid placing the tines in the row of loops that is closest to the edge of the sample. In the -45/+45 or -45/+15/+75 orientation, in the right column, we place the tines in the loops of the mesh where feasible, but due to the geometry of the mesh not all tines fit exactly into a loop. To reduce the likelihood of unraveling, we use a larger mesh area in this orientation.

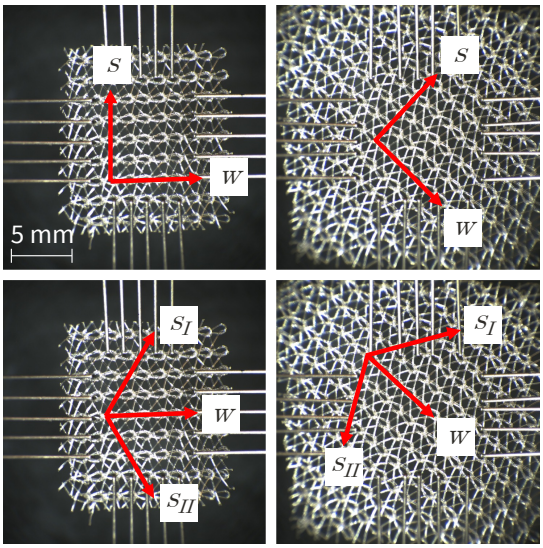

Figure 2: **Biaxial testing of the mesh in two orientations.** The top row shows the the two-fiber model with one warp and one shute direction $\boldsymbol{w}$ and $\boldsymbol{s}$, and the bottom row shows the three-fiber model with one warp and two shute directions $\boldsymbol{w}$ and $\boldsymbol{s}_I$ and $\boldsymbol{s}_{II}$. The left column illustrates the mesh in the 0/90 or 0/+60/-60 orientations, and the right column illustrates the mesh in the -45/+45 or -45/+15/+75 orientations.

We test a total of ten samples, five for each orientation [7]. Once we mount each sample into the device, we apply a 30 mN preload along both axes to establish a consistent reference configuration [49]. After preloading, we record the spacing between the tines as the gauge length, and perform five consecutive tests with 30 seconds of rest between each test [26]. Each test consists of linearly increasing the applied stretch for 100 seconds, followed by linearly decreasing the applied stretch for 100 seconds until the sample returns to its unstretched state. Table 1 summarizes the maximum stretches in each direction for each of the five tests. We perform all five tests on each of the ten samples. However, to minimize the effect of preload, we randomize the order of the tests for each sample.

Table 1: **Definition of five biaxial test settings.** Maximum stretches λ_1 and λ_2 for the five different tests of each sample. We increase the stretch linearly for 100 seconds until reaching the maximum stretch for each test, then decrease it linearly for 100 seconds to the undeformed configuration, and hold the sample in the undeformed configuration for 30 seconds between consecutive tests. To minimize the effect of preload, we randomize the order of the tests for each sample.

experiment	max stretch λ_1	max stretch λ_2
strip-x	1.10	1.00
off-x	1.10	1.05
equibiax	1.10	1.10
off-y	1.05	1.10
strip-y	1.00	1.10

2.2. Stress and strain analysis

We process the data from the CellScale BioTester 5000 to obtain the average Piola stress for given stretch values λ_1 and λ_2. First, we convert the force and displacement measurements to stresses and stretches. To do so, we measured the sample thickness t with calipers and set the gauge lengths L_1 and L_2 to the initial spacing between the tines in the 1- and 2-directions. Then, we computed the stretches λ_1 and λ_2 and the Piola stresses P_{11} and P_{22},

$$\lambda_1 = \frac{l_1}{L_1} \qquad \lambda_2 = \frac{l_2}{L_2} \qquad P_{11} = \frac{F_1}{L_2\, t} \qquad P_{22} = \frac{F_2}{L_1\, t} \tag{1}$$

where l_1 and l_2 are the measured gauge lengths and F_1 and F_2 are the measured forces in the 1- and 2-directions. The result are five loading and five unloading curves for each of the ten samples. We resample and average all curves at equidistant stretch intervals to obtain an averaged stress pair $\{P_{11}, P_{22}\}$ for each stretch pair $\{\lambda_1, \lambda_2\}$. Finally, for the samples mounted in the -45/+45 orientation, we use symmetry with respect to the diagonale and average the ten recorded stress-stretch curves to five distinct curves.

2.3. Kinematics

We characterize the deformation through the mapping $\boldsymbol{x} = \boldsymbol{\varphi}(\boldsymbol{X})$ that maps a point $\boldsymbol{X}$ in the reference configuration to a point $\boldsymbol{x}$ the deformed configuration. We then describe the local deformation using the deformation gradient,

$$\boldsymbol{F} = \nabla_X \boldsymbol{\varphi}(\boldsymbol{X})\,. \tag{2}$$

Multiplying $\boldsymbol{F}$ with its transpose $\boldsymbol{F}^{\mathrm{t}}$ introduces the symmetric right Cauchy Green deformation tensor $\boldsymbol{C}$,

$$\boldsymbol{C} = \boldsymbol{F}^{\mathrm{t}} \cdot \boldsymbol{F}\,. \tag{3}$$

To characterize the deformation of an orthotropic material, we introduce the three isotropic invariants, I_1, I_2, I_3, and a set of anisotropic invariants, I_{4i}, I_{8ij} [44, 28],

$$\begin{aligned}
I_1 &= [\boldsymbol{F}^{\mathrm{t}} \cdot \boldsymbol{F}] : \boldsymbol{I} & \partial_{\boldsymbol{F}} I_1 &= 2\boldsymbol{F} \\
I_2 &= \tfrac{1}{2}[I_1^2 - [\boldsymbol{F}^{\mathrm{t}} \cdot \boldsymbol{F}] : [\boldsymbol{F}^{\mathrm{t}} \cdot \boldsymbol{F}]] & \partial_{\boldsymbol{F}} I_2 &= 2I_1\boldsymbol{F} - 2\boldsymbol{F} \cdot \boldsymbol{F}^{\mathrm{t}} \cdot \boldsymbol{F} \\
I_3 &= \det(\boldsymbol{F}^{\mathrm{t}} \cdot \boldsymbol{F}) = J^2 & \partial_{\boldsymbol{F}} I_3 &= \det(\boldsymbol{F})\, \boldsymbol{F}^{-\mathrm{t}} \\
I_{4i} &= [\boldsymbol{F}^{\mathrm{t}} \cdot \boldsymbol{F}] : [\boldsymbol{n}_i \otimes \boldsymbol{n}_i] & \partial_{\boldsymbol{F}} I_{4\mathrm{i}} &= 2\boldsymbol{F} \cdot [\boldsymbol{n}_i \otimes \boldsymbol{n}_i] \\
I_{8ij} &= [\boldsymbol{F}^{\mathrm{t}} \cdot \boldsymbol{F}] : [\boldsymbol{n}_i \otimes \boldsymbol{n}_j]^{\mathrm{sym}} & \partial_{\boldsymbol{F}} I_{8ij} &= 2\boldsymbol{F} \cdot [\boldsymbol{n}_i \otimes \boldsymbol{n}_j]^{\mathrm{sym}}\,,
\end{aligned} \tag{4}$$

where $\boldsymbol{I}$ is the identity tensor, $\boldsymbol{n}_{i,j}$ with $i, j = 1, ..., n_{\mathrm{dir}}$ are the unit warp and shute directions in the undeformed reference configuration, and n_{dir} is the number of microstructural directions of our model. Since we are unable to measure the deformation in the thickness direction of the mesh, we assume that the mesh is perfectly incompressible, $I_3 = 1$.

In our biaxial extension tests, we stretch the sample in two orthogonal directions, $\lambda_1 \geq 1$ and $\lambda_2 \geq 1$. The incompressibility condition, $I_3 = \lambda_1^2\, \lambda_2^2\, \lambda_3^2 = 1$, defines the stretch in the thickness direction as $\lambda_3 = (\lambda_1\, \lambda_2)^{-1} \leq 1$. We assume that the deformation remains homogeneous and shear free, and the deformation gradient $\boldsymbol{F}$ remains diagonal,

$$\boldsymbol{F} = \mathrm{diag}\,\{\lambda_1, \lambda_2, (\lambda_1\lambda_2)^{-1}\}\,. \tag{5}$$

Next, we specify the invariants (4) in terms of the stretches λ_1 and λ_2 for two the microstructural architectures in Figures 1 and 2, the two-fiber model and the three-fiber model.

2.3.1. Two-fiber model

For the two-fiber model, we assume that we can represent the mesh through two orthogonal fiber families, one in the warp direction $\boldsymbol{w}$, and one in the shute direction $\boldsymbol{s}$, inclined against the warp direction by $\pi/2 = 90°$,

$$\begin{aligned}
\boldsymbol{w} &= [\ \cos(\alpha_w),\ \sin(\alpha_w), 0\,]^{\mathrm{t}} \\
\boldsymbol{s} &= [\ -\sin(\alpha_w), \cos(\alpha_w), 0\,]^{\mathrm{t}}\,,
\end{aligned} \tag{6}$$

where α_w is the warp angle, the angle of the warp direction against the 1-direction. We now specify the invariants (4) in terms of the biaxial stretches λ_1 and λ_2 and the warp angle α_w,

$$\begin{aligned}
I_1 &= \lambda_1^2 + \lambda_2^2 + (\lambda_1\lambda_2)^{-2} \\
I_2 &= \lambda_1^{-2} + \lambda_2^{-2} + (\lambda_1\lambda_2)^2 \\
I_{4w} &= \lambda_1^2\, \cos^2(\alpha_w) + \lambda_2^2\, \sin^2(\alpha_w) = \lambda_w^2 \\
I_{4s} &= \lambda_1^2\, \sin^2(\alpha_w) + \lambda_2^2\, \cos^2(\alpha_w) = \lambda_s^2 \\
I_{8ws} &= (\lambda_2^2 - \lambda_1^2)\sin(\alpha_w)\cos(\alpha_w)
\end{aligned} \tag{7}$$

and take their derivatives,

$$\begin{aligned}
\partial_{\boldsymbol{F}} I_1 &= 2\ \mathrm{diag}\ \{\lambda_1, \lambda_2, (\lambda_1\lambda_2)^{-1}\} \\
\partial_{\boldsymbol{F}} I_2 &= 2\ \mathrm{diag}\ \{\lambda_1\lambda_2^2 + \lambda_1^{-1}\lambda_2^{-2}, \lambda_1^2\lambda_2 + \lambda_1^{-2}\lambda_2^{-1}, \lambda_1\lambda_2^{-1} + \lambda_1^{-1}\lambda_2\} \\
\partial_{\boldsymbol{F}} I_{4w} &= 2\ \mathrm{diag}\ \{\lambda_1 \cos^2(\alpha_w), \lambda_2 \sin^2(\alpha_w), 0\} \\
\partial_{\boldsymbol{F}} I_{4s} &= 2\ \mathrm{diag}\ \{\lambda_1 \sin^2(\alpha_w), \lambda_2 \cos^2(\alpha_w), 0\} \\
\partial_{\boldsymbol{F}} I_{8ws} &= \mathrm{diag}\{-\lambda_1 \sin(2\alpha_w), \lambda_2 \sin(2\alpha_w), 0\}\,.
\end{aligned} \tag{8}$$

Our two-fiber model has five distinct invariants, I_1, I_2, I_{4w}, I_{4s}, I_{8ws}, where I_{4w} and I_{4s} take the interpretation of the squared stretches in the warp and shute directions λ_w and λ_s, and I_{8ws} characterizes the interaction between the warp and shute directions. For the special case of the 0/90 orientation, the anisotropic invariants are

$$I_{4w} = \lambda_1^2 \qquad I_{4s} = \lambda_2^2 \qquad I_{8ws} = 0\,, \tag{9}$$

and we already see that this setup is incapable of probing the interaction between the warp and shute directions since $I_{8ws} = 0$. For the special case of the +45/-45 orientation, the anisotropic invariants are

$$I_{4w} = \tfrac{1}{2}\,[\lambda_1^2 + \lambda_2^2] \quad I_{4s} = \tfrac{1}{2}\,[\lambda_1^2 + \lambda_2^2] \quad I_{8ws} = \tfrac{1}{2}\,[-\lambda_1^2 + \lambda_2^2]\,, \tag{10}$$

and we already see that this setup is incapable of distinguishing between the warp and shute directions since $I_{4w} = I_{4s}$.

2.3.2. Three-fiber model

The potential shortcomings of the two-fiber model motivate a more advanced three-fiber model with three fiber families, one in the warp direction $\boldsymbol{w}$, and two in the shute directions $\boldsymbol{s}_I$ and $\boldsymbol{s}_{II}$, symmetrically inclined against the warp direction by by $+\pi/3 = +60°$ and $-\pi/3 = -60°$,

$$\begin{aligned}
\boldsymbol{w} &= [\ \cos(\alpha_w), \quad \sin(\alpha_w), \quad 0\,]^{\mathrm{t}} \\
\boldsymbol{s}_I &= [\ \cos(\alpha_w + \tfrac{1}{3}\pi), \sin(\alpha_w + \tfrac{1}{3}\pi), 0\,]^{\mathrm{t}} \\
\boldsymbol{s}_{II} &= [\ \cos(\alpha_w - \tfrac{1}{3}\pi), \sin(\alpha_w - \tfrac{1}{3}\pi), 0\,]^{\mathrm{t}}
\end{aligned} \tag{11}$$

where α_w denotes the warp angle against the 1-direction. We now specify the invariants (4) in terms of the biaxial stretches λ_1 and λ_2 and the warp angle α_w,

$$\begin{aligned}
I_1 &= \lambda_1^2 + \lambda_2^2 + (\lambda_1\lambda_2)^{-2} \\
I_2 &= \lambda_1^{-2} + \lambda_2^{-2} + (\lambda_1\lambda_2)^{2} \\
I_{4w} &= \lambda_1^2 \cos^2(\alpha_w) + \lambda_2^2 \sin^2(\alpha_w) = \lambda_w^2 \\
I_{4s_I} &= \lambda_1^2 \cos^2(\alpha_w + \tfrac{1}{3}\pi) + \lambda_2^2 \sin^2(\alpha_w + \tfrac{1}{3}\pi) = \lambda_{s_I}^2 \\
I_{4s_{II}} &= \lambda_1^2 \cos^2(\alpha_w - \tfrac{1}{3}\pi) + \lambda_2^2 \sin^2(\alpha_w - \tfrac{1}{3}\pi) = \lambda_{s_{II}}^2 \\
I_{8ws_I} &= \lambda_1^2 \cos(\alpha_w)\cos(\alpha_w + \tfrac{1}{3}\pi) + \lambda_2^2 \sin(\alpha_w)\sin(\alpha_w + \tfrac{1}{3}\pi) \\
I_{8ws_{II}} &= \lambda_1^2 \cos(\alpha_w)\cos(\alpha_w - \tfrac{1}{3}\pi) + \lambda_2^2 \sin(\alpha_w)\sin(\alpha_w - \tfrac{1}{3}\pi) \\
I_{8s_Is_{II}} &= \lambda_1^2 \cos(\alpha_w + \tfrac{1}{3}\pi)\cos(\alpha_w - \tfrac{1}{3}\pi) \\
&\quad + \lambda_2^2 \sin(\alpha_w + \tfrac{1}{3}\pi)\sin(\alpha_w - \tfrac{1}{3}\pi)
\end{aligned} \tag{12}$$

Our three-fiber model has eight distinct invariants, I_1, I_2, I_{4w}, I_{4s_I}, $I_4 s_{II}$, I_{8ws_I}, $I_{8ws_{II}}$, $I_{8s_Is_{II}}$, where I_{4w}, I_{4s_I}, $I_{4s_{II}}$ take the interpretation of the squared stretches in the warp and shute directions λ_w, λ_{s_I}, $\lambda_{s_{II}}$ and I_{8ws_I}, $I_{8ws_{II}}$, $I_{8s_Is_{II}}$ characterizes the interaction between the warp and shute directions. For the special case of the 0/+60/-60 orientation, the anisotropic invariants are

$$\begin{aligned}
I_{4w} &= \lambda_1^2 & I_{4s_I} &= \tfrac{1}{4}[\,\lambda_1^2 + 3\lambda_2^2] & I_{4s_{II}} &= \tfrac{1}{4}[\lambda_1^2 + 3\lambda_2^2] \\
I_{8ws_I} &= \tfrac{1}{2}\lambda_1^2 & I_{8ws_{II}} &= \tfrac{1}{2}\,\lambda_1^2 & I_{8s_Is_{II}} &= \tfrac{1}{4}[\lambda_1^2 - 3\lambda_2^2]\,,
\end{aligned} \tag{13}$$

and we notice the microstructural symmetry of the two shute directions as $I_{4s_I} = I_{4s_{II}}$ and $I_{8ws_I} = I_{8ws_{II}}$. For the special case of the -45/+15/+75 orientation, the anisotropic invariants are

$$\begin{aligned}
I_{4w} &= [+\tfrac{1}{2}\qquad\qquad]\,\lambda_1^2 + [+\tfrac{1}{2}\qquad\qquad]\,\lambda_2^2 \\
I_{4s_I} &= [+\tfrac{1}{2} - \tfrac{1}{4}\sqrt{3}\,]\,\lambda_1^2 + [+\tfrac{1}{2} + \tfrac{1}{4}\sqrt{3}\,]\,\lambda_2^2 \\
I_{4s_{II}} &= [+\tfrac{1}{2} + \tfrac{1}{4}\sqrt{3}\,]\,\lambda_1^2 + [+\tfrac{1}{2} - \tfrac{1}{4}\sqrt{3}\,]\,\lambda_2^2 \\
I_{8ws_I} &= [+\tfrac{1}{4} - \tfrac{1}{4}\sqrt{3}\,]\,\lambda_1^2 + [+\tfrac{1}{4} + \tfrac{1}{4}\sqrt{3}\,]\,\lambda_2^2 \\
I_{8ws_{II}} &= [+\tfrac{1}{4} + \tfrac{1}{4}\sqrt{3}\,]\,\lambda_1^2 + [+\tfrac{1}{4} - \tfrac{1}{4}\sqrt{3}\,]\,\lambda_2^2 \\
I_{8s_Is_{II}} &= [-\tfrac{1}{4}\qquad\qquad]\,\lambda_1^2 + [-\tfrac{1}{4}\qquad\qquad]\,\lambda_2^2\,,
\end{aligned} \tag{14}$$

and we immediately notice that the three-fiber model invariants are much richer than the two-fiber model invariants.

2.4. Constitutive modeling

A constitutive model is a material-specific function that estimates the stress in a material given its deformation history. In the case of a hyperelastic constitutive model, the stress, in our case the Piola stress $\boldsymbol{P}$, only depends on the current deformation state, in our case the deformation gradient $\boldsymbol{F}$, such that $\boldsymbol{P} = \boldsymbol{P}(\boldsymbol{F})$. To satisfy thermodynamic consistency, we can express the stress as a function of the strain energy density ψ as $\boldsymbol{P} = \partial\psi(\boldsymbol{F})/\partial\boldsymbol{F}$, which we reformulate in terms of our set of invariants $\psi(I_1, I_2, I_3, I_{4i}, I_{8ij})$,

$$\boldsymbol{P} = \frac{\partial\psi}{\partial I_1}\frac{\partial I_1}{\partial \boldsymbol{F}} + \frac{\partial\psi}{\partial I_2}\frac{\partial I_2}{\partial \boldsymbol{F}} + \frac{\partial\psi}{\partial I_3}\frac{\partial I_3}{\partial \boldsymbol{F}} + \frac{\partial\psi}{\partial I_{4i}}\frac{\partial I_{4\mathrm{i}}}{\partial \boldsymbol{F}} + \frac{\partial\psi}{\partial I_{8ij}}\frac{\partial I_{8\mathrm{ij}}}{\partial \boldsymbol{F}}\,. \tag{15}$$

where $i, j = 1, ..., n_{\mathrm{dir}}$ is the number of microstructural directions of our model. We explicitly enforce incompressibility by selecting the term in the third invariant as $\psi(I_3) = -p\,[\,J - 1\,]$, such that $\partial\psi/\partial I_3 \cdot\ \partial I_3/\partial\boldsymbol{F} = -p\,\boldsymbol{F}^{-\mathrm{t}}$. Here p acts as a Lagrange multiplier that we determine from the zero-thickness-stress condition.

2.5. Biaxial testing

In biaxial extension tests, we stretch the sample in two orthogonal directions, $\lambda_1 \geq 1$ and $\lambda_2 \geq 1$, and, by incompressibility, $\lambda_3 = (\lambda_1\,\lambda_2)^{-1} \leq 1$. We assume that the deformation remains homogeneous and shear free, and that the resulting Piola stress $\boldsymbol{P}$ remains diagonal,

$$\boldsymbol{P} = \mathrm{diag}\,\{P_{11}, P_{22}, 0\}\,. \tag{16}$$

We use the isotropic first and second invariants $I_1 = \lambda_1^2 + \lambda_2^2 + (\lambda_1\lambda_2)^{-2}$ and $I_2 = \lambda_1^{-2} + \lambda_2^{-2} + (\lambda_1\lambda_2)^2$ from equation (7) and their derivatives from equation (8) to determine the pressure p from the zero-thickness-stress condition in the third direction,

$$P_{33} = 0 \quad \text{thus} \quad p = 2\frac{1}{\lambda_1^2\lambda_2^2}\frac{\partial\psi}{\partial I_1} + 2\left(\frac{1}{\lambda_1^2} + \frac{1}{\lambda_2^2}\right)\frac{\partial\psi}{\partial I_2}\,. \tag{17}$$

Equations (15) and (17) then provide an explicit analytical expression for the nominal stresses P_{11} and P_{22} in terms of the stretches λ_1 and λ_2 and the warp angle α_w.

2.5.1. Two-fiber model

For the two-fiber model, the free energy function is a function of five terms, $\psi = \psi(I_1, I_2, I_{4w}, I_{4s}, I_{8ws})$, and the nominal stresses P_{11} and P_{22} have five terms, one for each invariant,

$$\begin{aligned}
P_{11} &= 2\left(\lambda_1 - \frac{1}{\lambda_1^3\lambda_2^2}\right)\frac{\partial\psi}{\partial I_1} + 2\left(\lambda_1\lambda_2^2 - \frac{1}{\lambda_1^3}\right)\frac{\partial\psi}{\partial I_2} \\
&\quad + 2\,\lambda_1\cos^2(\alpha_{\mathrm{w}})\,\frac{\partial\psi}{\partial I_{4w}} + 2\,\lambda_1\sin^2(\alpha_{\mathrm{w}})\,\frac{\partial\psi}{\partial I_{4s}} \\
&\quad - \lambda_1\sin(2\alpha_{\mathrm{w}})\,\frac{\partial\psi}{\partial I_{8ws}} \\
P_{22} &= 2\left(\lambda_2 - \frac{1}{\lambda_1^2\lambda_2^3}\right)\frac{\partial\psi}{\partial I_1} + 2\left(\lambda_1^2\lambda_2 - \frac{1}{\lambda_2^3}\right)\frac{\partial\psi}{\partial I_2} \\
&\quad + 2\,\lambda_2\sin^2(\alpha_w)\,\frac{\partial\psi}{\partial I_{4w}} + 2\,\lambda_2\cos^2(\alpha_w)\,\frac{\partial\psi}{\partial I_{4s}} \\
&\quad + \lambda_2\sin(2\alpha_{\mathrm{w}})\,\frac{\partial\psi}{\partial I_{8ws}}.
\end{aligned} \tag{18}$$

Here we make an important observation: Counterintuitively, the eighth-invariant term, $\partial\psi/\partial I_{8ws}$, contributes negatively to the stresses in the 1-direction and positively to the stresses in the 2-direction. This contradicts our general intuition, and potentially violates the condition of material symmetry. We therefore drop the dependence on the eighth invariant and reduce our set of invariants to four, $\psi = \psi(I_1, I_2, I_{4w}, I_{4s})$. For the special case of the 0/90 orientation, with $\alpha_w = 0\,\pi = 0°$, the biaxial Piola stresses simplify to

$$\begin{aligned}
P_{11} &= 2\left(\lambda_1 - \frac{1}{\lambda_1^3\lambda_2^2}\right)\frac{\partial\psi}{\partial I_1} + 2\left(\lambda_1\lambda_2^2 - \frac{1}{\lambda_1^3}\right)\frac{\partial\psi}{\partial I_2} + 2\lambda_1\,\frac{\partial\psi}{\partial I_{4w}} \\
P_{22} &= 2\left(\lambda_2 - \frac{1}{\lambda_1^2\lambda_2^3}\right)\frac{\partial\psi}{\partial I_1} + 2\left(\lambda_1^2\lambda_2 - \frac{1}{\lambda_2^3}\right)\frac{\partial\psi}{\partial I_2} + 2\lambda_2\,\frac{\partial\psi}{\partial I_{4s}}\,.
\end{aligned} \tag{19}$$

For the special case of the -45/+45 orientation, with $\alpha_w = -\pi/4 = -45°$, the stresses are

$$
\begin{aligned}
P_{11} &= 2\left(\lambda_1 - \frac{1}{\lambda_1^3\lambda_2^2}\right)\frac{\partial\psi}{\partial I_1} + 2\left(\lambda_1\lambda_2^2 - \frac{1}{\lambda_1^3}\right)\frac{\partial\psi}{\partial I_2} + \lambda_1\left(\frac{\partial\psi}{\partial I_{4w}} + \frac{\partial\psi}{\partial I_{4s}}\right)\\
P_{22} &= 2\left(\lambda_2 - \frac{1}{\lambda_1^2\lambda_2^3}\right)\frac{\partial\psi}{\partial I_1} + 2\left(\lambda_1^2\lambda_2 - \frac{1}{\lambda_2^3}\right)\frac{\partial\psi}{\partial I_2} + \lambda_2\left(\frac{\partial\psi}{\partial I_{4w}} + \frac{\partial\psi}{\partial I_{4s}}\right).
\end{aligned}
\tag{20}
$$

2.5.2. Three-fiber model

For the three-fiber model, for similar reasons as above, we drop the dependence on the eighth invariants and reduce our set of invariants to five, $\psi = \psi(I_1, I_2, I_{4w}, I_{4s_I}, I_{4s_{II}})$. We now express the fourth invariants of the three-fiber model, I_{4w}, I_{4s_I}, $I_{4s_{II}}$, in terms of the invariants of the two-fiber model, I_{4w}, I_{4s}, I_{8ws}, $I_{4(\circ)} = I_{4w}\cos^2(\alpha_\circ) + I_s\sin^2(\alpha_\circ) + I_{8ws}\sin(2\alpha_\circ)$. For our specific three-fiber model, with $(\circ) = \{w, s_I, s_{II}\}$, and $\alpha_\circ = \{0, +\frac{1}{3}\pi, -\frac{1}{3}\pi\}$, this allows us express the nominal stresses P_{11} and P_{22} using equation (18),

$$
\begin{aligned}
P_{11} &= 2\left(\lambda_1 - \frac{1}{\lambda_1^3\lambda_2^2}\right)\frac{\partial\psi}{\partial I_1} + 2\left(\lambda_1\lambda_2^2 - \frac{1}{\lambda_1^3}\right)\frac{\partial\psi}{\partial I_2}\\
&+ 2\,\lambda_1\cos^2(\alpha_\mathrm{w})\left(\frac{\partial\psi}{\partial I_{4w}} + \frac{1}{4}\frac{\partial\psi}{\partial I_{4s_I}} + \frac{1}{4}\frac{\partial\psi}{\partial I_{4s_{II}}}\right)\\
&+ 2\,\lambda_1\sin^2(\alpha_\mathrm{w})\left(\frac{3}{4}\frac{\partial\psi}{\partial I_{4s_I}} + \frac{3}{4}\frac{\partial\psi}{\partial I_{4s_{II}}}\right)\\
&- \lambda_1\sin(2\alpha_\mathrm{w})\left(\frac{\sqrt{3}}{2}\frac{\partial\psi}{\partial I_{4s_I}} - \frac{\sqrt{3}}{2}\frac{\partial\psi}{\partial I_{4s_{II}}}\right)\\
P_{22} &= 2\left(\lambda_2 - \frac{1}{\lambda_1^2\lambda_2^3}\right)\frac{\partial\psi}{\partial I_1} + 2\left(\lambda_1^2\lambda_2 - \frac{1}{\lambda_2^3}\right)\frac{\partial\psi}{\partial I_2}\\
&+ 2\,\lambda_2\cos^2(\alpha_\mathrm{w})\left(\frac{\partial\psi}{\partial I_{4w}} + \frac{1}{4}\frac{\partial\psi}{\partial I_{4s_I}} + \frac{1}{4}\frac{\partial\psi}{\partial I_{4s_{II}}}\right)\\
&+ 2\,\lambda_2\sin^2(\alpha_\mathrm{w})\left(\frac{3}{4}\frac{\partial\psi}{\partial I_{4s_I}} + \frac{3}{4}\frac{\partial\psi}{\partial I_{4s_{II}}}\right)\\
&- \lambda_2\sin(2\alpha_\mathrm{w})\left(\frac{\sqrt{3}}{2}\frac{\partial\psi}{\partial I_{4s_I}} - \frac{\sqrt{3}}{2}\frac{\partial\psi}{\partial I_{4s_{II}}}\right).
\end{aligned}
\tag{21}
$$

For the special case of the 0/+60/-60 orientation, with $\alpha_w = 0\pi = 0°$, the biaxial Piola stresses become

$$
\begin{aligned}
P_{11} &= 2\left(\lambda_1 - \frac{1}{\lambda_1^3\lambda_2^2}\right)\frac{\partial\psi}{\partial I_1} + 2\left(\lambda_1\lambda_2^2 - \frac{1}{\lambda_1^3}\right)\frac{\partial\psi}{\partial I_2}\\
&\quad + \frac{1}{2}\lambda_1\left(4\frac{\partial\psi}{\partial I_{4w}} + \frac{\partial\psi}{\partial I_{4s_I}} + \frac{\partial\psi}{\partial I_{4s_{II}}}\right)\\
P_{22} &= 2\left(\lambda_2 - \frac{1}{\lambda_1^2\lambda_2^3}\right)\frac{\partial\psi}{\partial I_1} + 2\left(\lambda_1^2\lambda_2 - \frac{1}{\lambda_2^3}\right)\frac{\partial\psi}{\partial I_2}\\
&\quad + \frac{3}{2}\lambda_1\left(\frac{\partial\psi}{\partial I_{4s_I}} + \frac{\partial\psi}{\partial I_{4s_{II}}}\right).
\end{aligned}
\tag{22}
$$

For the special case of the -45/+15/+75 orientation, with $\alpha_w = -\pi/4 = -45°$, the biaxial Piola stresses are

$$
\begin{aligned}
P_{11} &= 2\left(\lambda_1 - \frac{1}{\lambda_1^3\lambda_2^2}\right)\frac{\partial\psi}{\partial I_1} + 2\left(\lambda_1\lambda_2^2 - \frac{1}{\lambda_1^3}\right)\frac{\partial\psi}{\partial I_2}\\
&\quad + \lambda_1\left(\frac{\partial\psi}{\partial I_{4w}} + \left(1 + \frac{\sqrt{3}}{2}\right)\frac{\partial\psi}{\partial I_{4s_I}} + \left(1 - \frac{\sqrt{3}}{2}\right)\frac{\partial\psi}{\partial I_{4s_{II}}}\right)\\
P_{22} &= 2\left(\lambda_2 - \frac{1}{\lambda_1^2\lambda_2^3}\right)\frac{\partial\psi}{\partial I_1} + 2\left(\lambda_1^2\lambda_2 - \frac{1}{\lambda_2^3}\right)\frac{\partial\psi}{\partial I_2}\\
&\quad + \lambda_2\left(\frac{\partial\psi}{\partial I_{4w}} + \left(1 - \frac{\sqrt{3}}{2}\right)\frac{\partial\psi}{\partial I_{4s_I}} + \left(1 + \frac{\sqrt{3}}{2}\right)\frac{\partial\psi}{\partial I_{4s_{II}}}\right).
\end{aligned}
\tag{23}
$$

2.6. Constitutive neural networks

Motivated by the previous considerations, we design two constitutive neural networks to learn the free energy function ψ, a two-fiber network based on four invariants and a three-fiber network based on five invariants.

2.6.1. Two-fiber network

Our first neural network approximates a strain energy function in terms of four invariants I_1, I_2, I_{4w}, I_{4s} and has 28 parameters or network weights, $\boldsymbol{w} = \{w_1, ..., w_{14}; w_1^*, ..., w_{14}^*\}$, 14 internal weights w_i^* between its two hidden layers and 14 external weights w_i out of its final hidden layer. We assume that the individual contributions to the free energy are fully decoupled. For the isotropic terms $\psi(I_1)$ and $\psi(I_2)$, we adapt an isotropic constitutive neural network initially designed for rubber-like materials [19]. For the anisotropic terms $\psi(I_{4w})$ and $\psi(I_{4s})$, we adapt an anisotropic constitutive neural network initially designed for arteries [35], with the additional constraint that the linear and exponential linear terms in the warp direction, $-w_9 w_9^*[I_{4w} - 1]$ and $w_9[\exp(w_9^*[I_4 - 1]) - 1]$, and in the shute direction, $-w_{12}w_{12}^*[I_{4s} - 1]$ and $w_{12}[\exp(w_{12}^*[I_4 - 1]) - 1]$, are not independent but share the same weights [51]. The free energy function for the two-fiber network takes the following explicit form,

$$
\begin{aligned}
\psi = {} & w_1\ w_1^*\ [I_1\ -3] + w_2\ [\exp(w_2^*\ [I_1\ -3]\ ) - 1]\\
& + w_3\ w_3^*\ [I_1\ -3]^2 + w_4\ [\exp(w_4^*\ [I_1\ -3]^2) - 1]\\
& + w_5\ w_5^*\ [I_2\ -3] + w_6\ [\exp(w_6^*\ [I_2\ -3]\ ) - 1]\\
& + w_7\ w_7^*\ [I_2\ -3]^2 + w_8\ [\exp(w_8^*\ [I_2\ -3]^2) - 1]\\
& - w_9\ w_9^*\ [I_{4w} - 1] + w_9\ [\exp(w_9^*\ [I_{4w} - 1]\ ) - 1]\\
& + w_{10}\, w_{10}^*\, [I_{4w} - 1]^2 + w_{11}\, [\exp(w_{11}^*\, [I_{4w} - 1]^2) - 1]\\
& - w_{12}\, w_{12}^*\, [I_{4s} - 1] + w_{12}\, [\exp(w_{12}^*\, [I_{4s} - 1]\ ) - 1]\\
& + w_{13}\, w_{13}^*\, [I_{4s} - 1]^2 + w_{14}\, [\exp(w_{14}^*\, [I_{4s} - 1]^2) - 1].
\end{aligned}
\tag{24}
$$

Figure 3 summarizes the architecture of the two-fiber family constitutive neural network.

2.6.2. Three-fiber architecture

Our second model architecture approximates a strain energy function in terms of five invariants I_1, I_2, I_{4w}, I_{4sI}, I_{4sII} and has 28 parameters or network weights, $\boldsymbol{w} = \{w_1, ..., w_{14}; w_1^*, ..., w_{14}^*\}$, 14 internal weights w_i^* between its two hidden layers and 14 external weights w_i out of its final hidden layer. We use a similar neural network as before, and assume that the two shute directions $\boldsymbol{s}_I$ and s_{II} have the same microstructure and share the

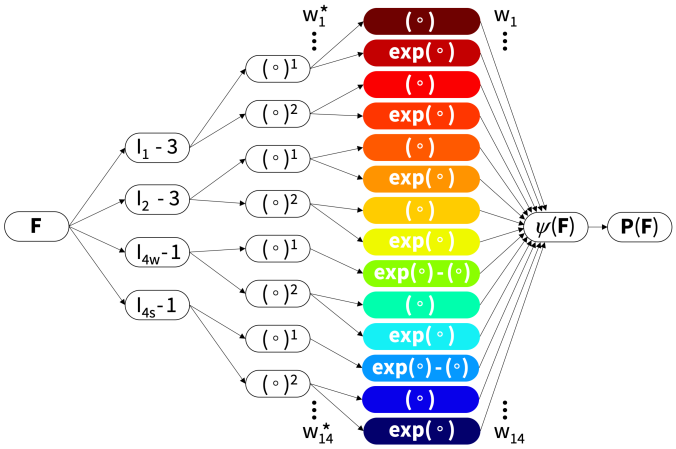

Figure 3: **Two-fiber constitutive neural network.** The network takes the two isotropic invariants I_1 and I_2 and the two anisotropic invariants I_{4w} and I_{4s} of the warp and shute directions $\boldsymbol{w}$ and $\boldsymbol{s}$ as input. The first layer generates powers $(\circ)$ and $(\circ)^2$ of the input and the second layer applies the identity $(\circ)$ and exponential function $(\exp(\circ))$ to these powers. The network learns the free energy function ψ as the weighted sum of the final layer, from which it derives the stress $\boldsymbol{P}$.

same weights w_{12}, w_{13}, w_{14} and $w^*_{12}, w^*_{13}, w^*_{14}$. The free energy function for the three-fiber network takes the following explicit form,

$$\begin{aligned}
\psi = {} & w_1\ w_1^*\ [I_1 \quad -3] + w_2\ [\exp(w_2^*\ [I_1 \quad -3]\ ) - 1] \\
& + w_3\ w_3^*\ [I_1 \quad -3]^2 + w_4\ [\exp(w_4^*\ [I_1 \quad -3]^2) - 1] \\
& + w_5\ w_5^*\ [I_2 \quad -3] + w_6\ [\exp(w_6^*\ [I_2 \quad -3]\ ) - 1] \\
& + w_7\ w_7^*\ [I_2 \quad -3]^2 + w_8\ [\exp(w_8^*\ [I_2 \quad -3]^2) - 1] \\
& - w_9\ w_9^*\ [I_{4w} \ -1] + w_9\ [\exp(w_9^*\ [I_{4w} \ -1]\ ) - 1] \\
& + w_{10}\, w_{10}^*\, [I_{4w} \ -1]^2 + w_{11}\, [\exp(w_{11}^*\, [I_{4w} \ -1]^2) - 1] \\
& - w_{12}\, w_{12}^*\, [I_{4s_I} \ -1] + w_{12}\, [\exp(w_{12}^*\, [I_{4s_I} \ -1]\ ) - 1] \\
& + w_{13}\, w_{13}^*\, [I_{4s_I} \ -1]^2 + w_{14}\, [\exp(w_{14}^*\, [I_{4s_I} \ -1]^2) - 1] \\
& - w_{12}\, w_{12}^*\, [I_{4s_{II}} -1] + w_{12}\, [\exp(w_{12}^*\, [I_{4s_{II}} -1]\ ) - 1] \\
& + w_{13}\, w_{13}^*\, [I_{4s_{II}} -1]^2 + w_{14}\, [\exp(w_{14}^*\, [I_{4s_{II}} -1]^2) - 1]\,.
\end{aligned} \tag{25}$$

Figure 4 summarizes the architecture of the three-fiber family constitutive neural network.

2.7. Model training

To discover models and parameters $\boldsymbol{w} = \{w_1, ..., w_{14}; w_1^*, ..., w_{14}^*\}$ that best describe our synthetic mesh, we use the Adam optimizer to perform gradient descent on a weighted least squared error loss function L that penalizes the error between the discovered model $\boldsymbol{P}(\boldsymbol{F}_i, \boldsymbol{w})$ and the experimental data $\hat{\boldsymbol{P}}_i$ at $i = 1, ..., n_{\text{data}}$ discrete points, supplemented by L_p regularization,

$$L(\boldsymbol{w}; \boldsymbol{F}) = \frac{1}{n_{\text{data}}} \sum_{i=1}^{n_{\text{data}}} \left\| \frac{\boldsymbol{P}(\boldsymbol{F}_i, \boldsymbol{w}) - \hat{\boldsymbol{P}}_i}{P_{\max}} \right\|^2 + L_p(\boldsymbol{w}) \rightarrow \min_{\boldsymbol{w}}\,. \tag{26}$$

To account for all experiments equally, we weigh the error of each of the stress-stretch curve by the inverse of its maximum stress $P_{\max}$ [25]. For the L_0 regularization, we supplement the loss function by an α-weighted regularization term, $L_0 = \alpha \| \boldsymbol{w} \|_0$ with $\| \boldsymbol{w} \|_0 = \sum_{i=1}^{n_w} I(w_i \neq 0)$, where $I(\circ)$ is the indicator function that is one if the condition inside the parenthesis is true and zero otherwise. In practice, instead of solving the full discrete combinatorial problem and exploring all possible $2^{14} = 16,384$ combinations of terms, we only explore the weights and losses of the possible 14 one-term models and 91 two-term models by explicitly setting all other terms to zero. For the $L_{0.5}$ regularization, we supplement the loss function by an α-weighted regularization, $L_{0.5} = \alpha \| \boldsymbol{w} \|_{0.5}^{0.5}$ with $\| \boldsymbol{w} \|_{0.5}^{0.5} = \sum_{i=1}^{14} \sqrt{|P_i(w_i, w_i^*)|}$, where P_i is the color-coded area of the stress contribution of the i-th term across all loading modes that we compute by summing the strain energies at the maximum displacement for each loading mode. The penalty parameter α sets the strength of the $L_{0.5}$ regularization. We increase α progressively until the fit of the model to the data starts to become noticeably worse. To minimize the training time and ensure that the initial model creates predictions that are of the same order of magnitude as the data, we initialize all weights with a uniform distribution $\boldsymbol{w} =\sim \text{Uniform}([0, \gamma))$, where we choose γ such that ,in expectation, the total area under the measured stress-stretch curve equals the total area under the predicted stress-stretch curve.

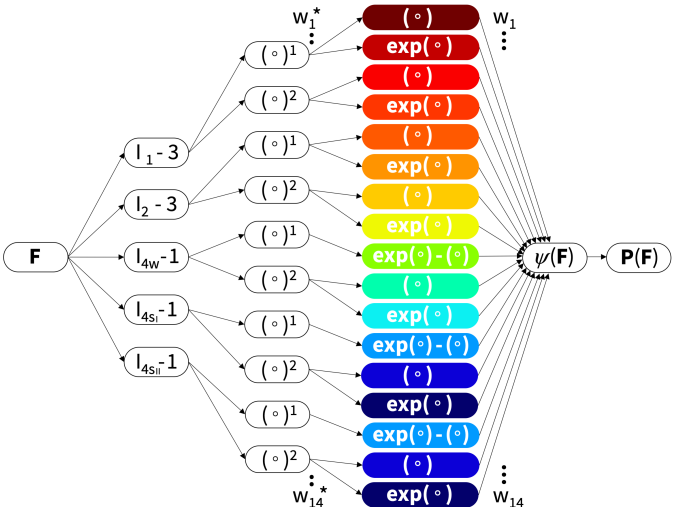

Figure 4: **Three-fiber constitutive neural network.** The network takes the two isotropic invariants I_1 and I_2 and the three anisotropic invariants I_{4w} and I_{4s_I} and $I_{4s_{II}}$ of the warp and shute directions $\boldsymbol{w}$ and $\boldsymbol{s}_I$ and $\boldsymbol{s}_{II}$ as input. The first layer generates powers $(\circ)$ and $(\circ)^2$ of the input and the second layer applies the identity $(\circ)$ and exponential function $(\exp(\circ))$ to these powers. The network learns the free energy function ψ as the weighted sum of the final layer, from which it derives the stress $\boldsymbol{P}$. We assume that the two shute directions $\boldsymbol{s}_I$ and $\boldsymbol{s}_{II}$ have the same microstructure and share the same weights.

3. Results

We perform all experiments as described in Section 2.1 and examine the data for each individual experiment. Figures 5 and 6 show the loading and unloading curves for the 0/90 orientation in the top two rows and for the -45/+45 orientation in the bottom row. The solid lines represent the means of $n = 5$ tests and the shaded areas represent the standard deviations. In all experiments, we observe significant hysteresis between the

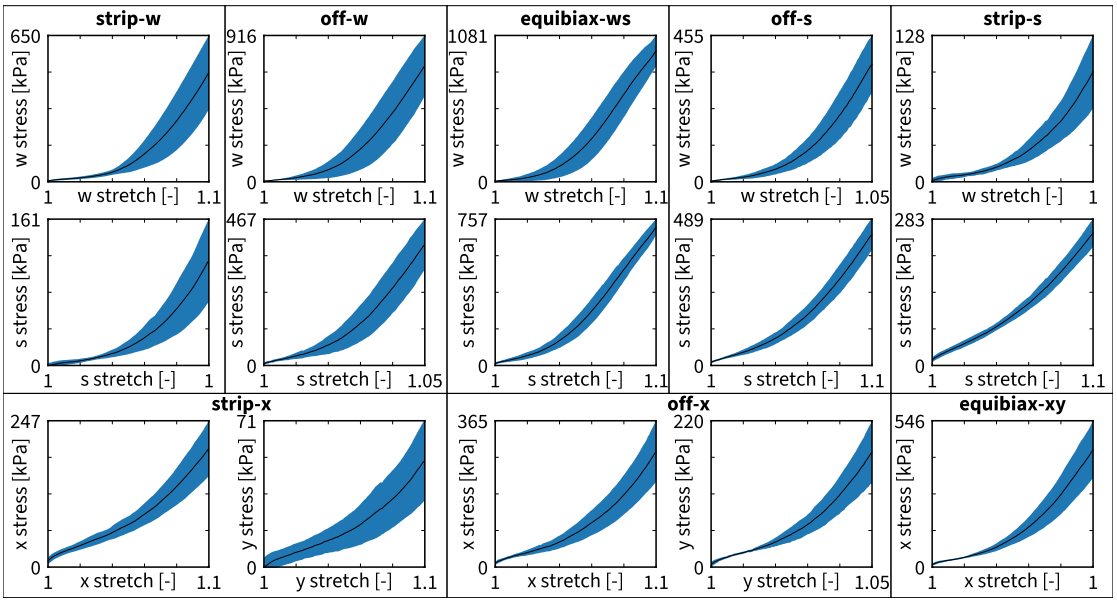

Figure 5: **Biaxial test data during loading.** Warp and shute stress-stretch data for strip-x, off-x, equibiax, off-y, and strip-y tests in the 0/90 orientation, top rows, and in the -45/+45 orientation, bottom row. Solid lines represent the means of $n = 5$ tests, shaded areas represent the standard deviations.

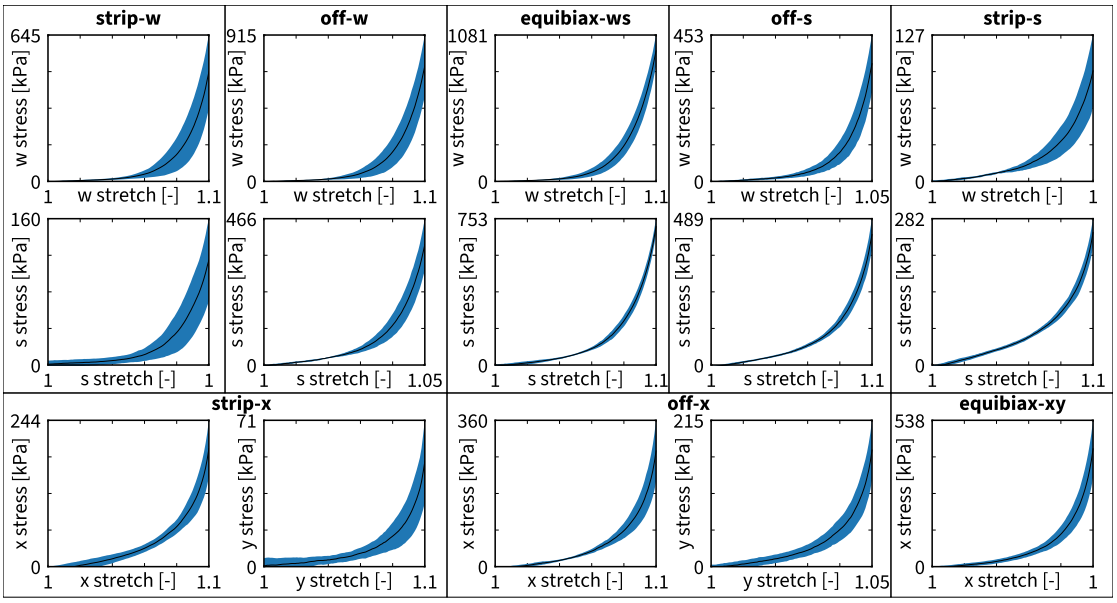

Figure 6: **Biaxial test data during unloading.** Stress-stretch data for strip-x, off-x, equibiax, off-y, and strip-y tests in the 0/90 orientation, top rows, and in the -45/+45 orientation, bottom row. Solid lines represent the means of $n = 5$ tests, shaded areas represent the standard deviations.

loading and unloading curves. The stress remains constant during the thirty-second holding between each experiment, from which we conclude that the difference in loading and unloading is a result of microstructural rearrangements of the mesh, rather than a viscous effect. For model discovery, for each experiment type, we extract the stretches and average stresses across the $n = 5$ tests during loading and unloading and summarize the stretch-stress data of all ten experiments in Table 2.

3.1. Mechanical signature of warp knitted fabric

All fifteen stress-stretch curves in Figures 5 and 6 display a similar trend: During the first half of the loading interval, the mesh behaves very compliant and the recorded stresses remain low; during the second half, the mesh stiffens and the stresses increase exponentially. Although present during both loading and unloading, this trend is less visible in the loading curves in Figure 5 than in the unloading curves in Figure 6, which also display smaller standard deviations. Intuitively, we expect the mesh to be stiffer in the warp than in the shute direction and Figures 5 and 6 and Table 2 confirm our expectation: In the strip-w and strip-s tests, the peak warp stress of 484 kPa is about twice as large as the peak shute stress of 256 kPa. In the equibiaxial test, the peak warp stress of 966 kPa is about one third larger than the peak shute stress of 714 kPa. We also expect the mesh

Table 2: **Biaxial test data.** Stress-stretch data for strip-x, off-x, equibiax, off-y, and strip-y tests in the 0/90 orientation, top , and in the -45/+45 orientation, bottom. Stress values are the means of $n = 5$ loading and unloading tests.

0/90 orientation strip-w			**0/90 orientation off-w**			**0/90 orientation equi-biax**			**0/90 orientation off-s**			**0/90 orientation strip-s**		
$\lambda_w : \lambda_s = 1.10 : 1.00$			$\lambda_w : \lambda_s = 1.10 : 1.05$			$\lambda_w : \lambda_s = 1.10 : 1.10$			$\lambda_w : \lambda_s = 1.05 : 1.10$			$\lambda_w : \lambda_s = 1.00 : 1.10$		
λ_w [-]	σ_w [kPa]	σ_s [kPa]	λ_w [-]	σ_w [kPa]	σ_s [kPa]	λ_w [-]	σ_w [kPa]	σ_s [kPa]	λ_s [-]	σ_w [kPa]	σ_s [kPa]	λ_s [-]	σ_w [kPa]	σ_s [kPa]
1.000	0.00	0.00	1.000	0.00	0.00	1.000	0.00	0.00	1.000	0.00	0.00	1.000	0.00	0.00
1.006	4.49	1.59	1.006	4.88	6.88	1.006	5.68	10.01	1.006	2.82	8.59	1.006	1.76	10.05
1.013	7.12	2.70	1.013	8.82	11.91	1.013	10.11	18.32	1.013	5.41	16.36	1.013	3.00	17.28
1.019	9.68	3.54	1.019	13.66	17.67	1.019	16.06	27.79	1.019	8.16	24.28	1.019	3.94	24.33
1.025	12.93	4.72	1.025	19.45	23.20	1.025	24.63	38.59	1.025	11.59	33.14	1.025	5.11	31.47
1.031	17.01	6.14	1.031	27.21	30.27	1.031	36.91	53.24	1.031	16.10	43.14	1.031	6.77	39.30
1.038	22.62	7.97	1.038	38.38	39.25	1.038	55.25	71.20	1.038	21.61	54.36	1.038	8.79	47.74
1.044	31.55	10.21	1.044	53.89	50.07	1.044	80.88	94.46	1.044	28.99	67.80	1.044	11.37	57.02
1.050	44.58	13.31	1.050	74.58	62.77	1.050	114.03	122.29	1.050	38.82	84.24	1.050	14.41	67.33
1.056	62.93	17.64	1.056	103.79	79.64	1.056	157.77	156.84	1.056	52.57	103.39	1.056	18.01	78.80
1.063	86.50	23.21	1.063	140.76	99.45	1.063	213.88	198.11	1.063	69.17	126.07	1.063	23.21	91.84
1.069	116.72	29.97	1.069	187.30	124.63	1.069	283.90	247.19	1.069	90.47	153.03	1.069	29.22	107.24
1.075	155.29	39.31	1.075	247.71	156.25	1.075	370.58	306.65	1.075	119.61	185.94	1.075	36.77	124.38
1.081	204.50	51.40	1.081	322.51	193.98	1.081	473.17	374.49	1.081	155.46	225.04	1.081	45.75	145.31
1.088	269.71	67.25	1.088	421.10	240.98	1.088	598.90	456.81	1.088	203.65	275.28	1.088	57.79	171.06
1.094	357.00	87.38	1.094	548.29	301.55	1.094	753.88	561.17	1.094	270.62	340.53	1.094	74.18	204.12
1.100	484.04	115.51	1.100	724.81	385.76	1.100	966.14	714.12	1.100	365.55	437.14	1.100	96.21	256.15

-45/+45 orientation strip-x			**-45/+45 orientation off-x**			**-45/+45 orientation equi-biax**			**-45/+45 orientation off-y**			**-45/+45 orientation strip-y**		
$\lambda_x : \lambda_y = 1.10 : 1.00$			$\lambda_x : \lambda_y = 1.10 : 1.05$			$\lambda_x : \lambda_y = 1.10 : 1.10$			$\lambda_x : \lambda_y = 1.05 : 1.10$			$\lambda_x : \lambda_y = 1.00 : 1.05$		
λ_x [-]	σ_x [kPa]	σ_y [kPa]	λ_x [-]	σ_x [kPa]	σ_y [kPa]	λ_x [-]	σ_x [kPa]	σ_y [kPa]	λ_y [-]	σ_x [kPa]	σ_y [kPa]	λ_y [-]	σ_x [kPa]	σ_y [kPa]
1.000	0.00	0.00	1.000	0.00	0.00	1.000	0.00	0.00	1.000	0.00	0.00	1.000	0.00	0.00
1.006	9.70	2.08	1.006	8.78	6.80	1.006	9.96	9.96	1.006	6.80	8.78	1.006	2.08	9.70
1.013	15.58	3.36	1.013	14.45	10.71	1.013	15.61	15.61	1.013	10.71	14.45	1.013	3.36	15.58
1.019	20.89	4.33	1.019	19.82	14.15	1.019	21.62	21.62	1.019	14.15	19.82	1.019	4.33	20.89
1.025	26.47	5.26	1.025	25.66	17.83	1.025	28.56	28.56	1.025	17.83	25.66	1.025	5.26	26.47
1.031	32.24	6.31	1.031	31.86	21.74	1.031	36.47	36.47	1.031	21.74	31.86	1.031	6.31	32.24
1.038	38.30	7.32	1.038	38.95	25.78	1.038	45.83	45.83	1.038	25.78	38.95	1.038	7.32	38.30
1.044	45.41	8.44	1.044	47.91	30.97	1.044	58.50	58.50	1.044	30.97	47.91	1.044	8.44	45.41
1.050	53.15	9.83	1.050	58.33	37.14	1.050	73.30	73.30	1.050	37.14	58.33	1.050	9.83	53.15
1.056	62.09	11.48	1.056	70.30	44.19	1.056	91.43	91.43	1.056	44.19	70.30	1.056	11.48	62.09
1.063	72.81	13.81	1.063	84.18	52.68	1.063	113.37	113.37	1.063	52.68	84.18	1.063	13.81	72.81
1.069	85.34	16.47	1.069	101.18	62.96	1.069	138.85	138.85	1.069	62.96	101.18	1.069	16.47	85.34
1.075	100.14	19.79	1.075	121.49	75.30	1.075	170.42	170.42	1.075	75.30	121.49	1.075	19.79	100.14
1.081	117.90	23.78	1.081	146.91	90.74	1.081	211.22	211.22	1.081	90.74	146.91	1.081	23.78	117.90
1.088	140.27	29.07	1.088	178.91	109.49	1.088	262.98	262.98	1.088	109.49	178.91	1.088	29.07	140.27
1.094	169.38	36.57	1.094	223.03	136.23	1.094	328.39	328.39	1.094	136.23	223.03	1.094	36.57	169.38
1.100	218.89	50.19	1.100	297.23	181.10	1.100	441.78	441.78	1.100	181.10	297.23	1.100	50.19	218.89

to be stiffer in the 0/90 orientation, for which the loading axes are aligned with the warp and shute directions, than in the -45/+45 orientation, for which the loading axes are rotated by 45 degrees against the warp and shute directions. In the strip-x and strip-y tests, the peak stress of 219 kPa is significantly lower than either of the two peak stresses of 484 kPa and 256 kPa of the unrotated setting. In the equibiaxial test, the peak stress of 442 kPa is also lower than two biaxial peak stresses of 966 kPa and 714 kPa of the unrotated setting. Taken together, our measurements confirm that knitted meshes display unique mechanical properties including an remarkable *initial flexibility*, a pronounced *nonlinear stiffening*, and an *extreme anisotropy*. To gain further insights into these characteristics, we now analyze the data using our constitutive neural networks and discover the two- and three-fiber models that best characterize our mesh.

3.2. Two-fiber architecture

First, we train the full network using the two-fiber architecture in Figure 3. We initialize the model parameters randomly and train the network without any regularization. Then, we use these trained parameters to re-initialize the parameters and train the network using $L_{0.5}$ regularization with a regularization parameter $\alpha = 0.001$. We use data from all experiments for training. Figure 7 shows the discovered model, with the contributions of each discovered stress term in a different color. The network discovers four non-zero terms, one is the exponential

linear first invariant I_1 Demiray term [5], one is a quadratic first invariant I_1 term, and two are the exponential quadratic fourth warp and shute invariant I_{4w} and I_{4s} Holzapfel terms [11],

$$\psi = \tfrac{1}{2}a_1[\exp(b_1[I_1 - 3])\ \text{-1}]/b_1 + \tfrac{1}{2}\mu_1[I_1 - 3]^2 + \tfrac{1}{2}a_2[\exp(b_2[I_{4w}\ \text{-1}]^2)\ \text{-1}]/b_2 + \tfrac{1}{2}a_3[\exp(b_3[I_{4s}\ \text{-1}]^2)\ \text{-1}]/b_3$$

where the stiffness-like parameters are $a_1 = 91.24$ kPa, $\mu_1 = 3794$ kPa, $a_2 = 3.31$ kPa, $a_3 = 5.30$ kPa, and the nonlinearity parameters are $b_1 = 0.17$, $b_2 = 127.20$, $b_3 = 94.68$. Figure 7 illustrates the discovered two-fiber model along with the biaxial test data. It highlights four different terms in four characteristic colors and quantifies the goodness of all 15 fits in terms of the R^2 values. The individual stress-stretch plots suggest that the discovered model performs fairly well on the experiments in the 0/90 orientation, but performs poorly on the strip-x experiment in the -45/+45 orientation, where it significantly underpredicts the x-stress and over-predicts the y-stress. This reduces the mean R^2 value across all tests to 0.7573.

Additionally, we train a subset of the network in Figure 3 with *only anisotropic* terms. To do this, we constrain the weights of all eight isotropic terms to equal zero, $w_1, ..., w_8 = 0$. We again use $L_{0.5}$ regularization with a regularization parameter $\alpha = 0.001$ and use all data for training. Figure 8 shows the discovered two-fiber model with no isotropic terms. The network discovers two anisotropic terms, both are the exponential linear Weiss terms [51], one in the fourth warp invariant I_{4w} and one in the fourth shute invariant I_{4s},

$$\psi = \tfrac{1}{2}a_1\,[\exp(b_1[I_{4w} - 1]) - 1]/b_1 - \tfrac{1}{2}a_1\,[I_{4w} - 1] + \tfrac{1}{2}a_2\,[\exp(b_2[I_{4s} - 1]) - 1]/b_2 - \tfrac{1}{2}a_2\,[I_{4s} - 1]$$

with the two stiffness-like parameters $a_1 = 2.998$ kPa, $a_2 = 9.811$ kPa, and the two nonlinearity parameters $b_1 = 21.07$, $b_2 = 12.63$. Notably, the fit of this model is extremely poor. The mean R^2 value across all tests is as low as 0.5104, and five tests have R^2 values of zero. We conclude that the orthotropic two-fiber model with no isotropic terms fails to accurately describe the behavior of the mesh.

Next, instead of sparsifying the model and reducing the number of terms with $L_{0.5}$ regularization, we use L_0 regularization to identify the best one- and two-term models by sampling all 14 single terms and all 91 pairs of two terms and minimizing the mean squared error of the 105 models. Figure 9 shows the minimized loss for all 105 combination of terms with the one-term models on the diagonale and the two-term models off the diagonale. For the two-fiber architecture, the best-in-class two-term model consists of one isotropic term, the exponential linear first invariant I_1 Demiray [5], and one anisotropic term, the exponential quadratic fourth warp invariant I_{4w} Holzapfel term [11],

$$\psi = \tfrac{1}{2}a_1\,[\exp(b_1[I_1 - 3])\ -1]/b_1 + \tfrac{1}{2}a_2\,[\exp(b_2[I_{4w} - 1]^2)\ -1]/b_2\,,$$

with the two stiffness-like parameters $a_1 = 25.20$ kPa and $a_2 = 0.40$ kPa, and the two nonlinearity parameters $b_1 = 17.30$ and $b_2 = 127.30$, and achieves a training loss of 0.077. Strikingly, while the data suggest that the mesh is highly anisotropic, the models with only anisotropic terms perform the worst.

3.3. Three-fiber architecture

Second, we train the full network using the three-fiber architecture in Figure 4. Again, we initialize the model parameters randomly and train the network without any regularization. Then, we use these trained parameters to re-initialize the parameters and train the network using $L_{0.5}$ regularization with a regularization parameter $\alpha = 0.001$. We use data from all experiments for training. Figure 10 shows the discovered model, with the contributions of each discovered stress term in a different color. The network discovers three non-zero terms, one is the exponential quadratic first invariant I_1 Holzapfel term [11], and two are the exponential linear fourth warp and shute invariants I_{4w} and I_{4s_I} and $I_{4s_{II}}$ Weiss terms [51],

$$\psi = \tfrac{1}{2}a_1[\exp(b_1[I_1 - 3]^2)\ -1]/b_1 + \tfrac{1}{2}a_2[\exp(b_2[I_{4w} - 1])\ -1]/b_2 - \tfrac{1}{2}a_2[I_{4w} - 1] + \tfrac{1}{2}a_3[\exp(b_3[I_{4s_{I,II}} - 1])\ -1]/b_3 - \tfrac{1}{2}a_3[I_{4s_{I,II}} - 1]$$

where the stiffness-like parameters are $a_1 = 2427$ kPa, $a_2 = 0.16$ kPa, $a_3 = 81.77$ kPa, and the nonlinearity parameters are $b_1 = 0.51$, $b_2 = 37.65$, $b_3 = 4.78$. Figure 10 shows the discovered three-fiber model along with the biaxial test data. Similar to the two-fiber model in Figure 7, the three-fiber model performs fairly well on the experiments in the 0/90 orientation. However, in contrast to the two-fiber model, the three-fiber model also performs well on the strip-x experiment in the +45/-45 orientation and achieves an R^2 of 0.98 in the x-direction and 0.93 in the y-direction compared to the two-fiber model with only 0.67 in the x-direction and 0.10 in the y-direction. Its mean R^2 value across all tests is 0.8614.

Additionally, we train a subset of the network in Figure 4 with *only anisotropic* terms. Again, we constrain the weights of all eight isotropic terms to equal zero, $w_1, ..., w_8 = 0$, use $L_{0.5}$ regularization with $\alpha = 0.001$, and use all data for training. Figure 11 shows the discovered three-fiber model with no isotropic terms. Similar to the two-term case, the network discovers two anisotropic terms, both are exponential linear Weiss terms [51], one in the fourth warp invariant I_{4w} and one in the fourth shute invariants I_{4s_I} and $I_{4s_{II}}$,

$$\psi = \tfrac{1}{2}a_1\,[\exp(b_1[I_{4w}\ -1]) - 1]/b_1 - \tfrac{1}{2}a_1\,[I_{4w} - 1] + \tfrac{1}{2}a_2\,[\exp(b_2(I_{4s_{I,II}} - 1]) - 1]/b_2 - \tfrac{1}{2}a_2\,]I_{4s_{I,II}} - 1]$$

with the two stiffness-like parameters, $a_1 = 1.26$ kPa, $a_2 = 28.93$ kPa, and the two nonlinearity parameters $b_1 = 24.55$, $b_2 = 7.20$. Notably, the anisotropic three-fiber model in Figure 11 with a mean R^2 value of 0.8199 provides a much better fit to the data than the anisotropic two-fiber model in Figure 8 with a mean R^2 value of 0.5104, and, without any isotropic terms, performs almost as good as the three-fiber model in Figure 10 with a mean R^2 value of 0.8614.

Finally, we use L_0 regularization to identify the best one- and

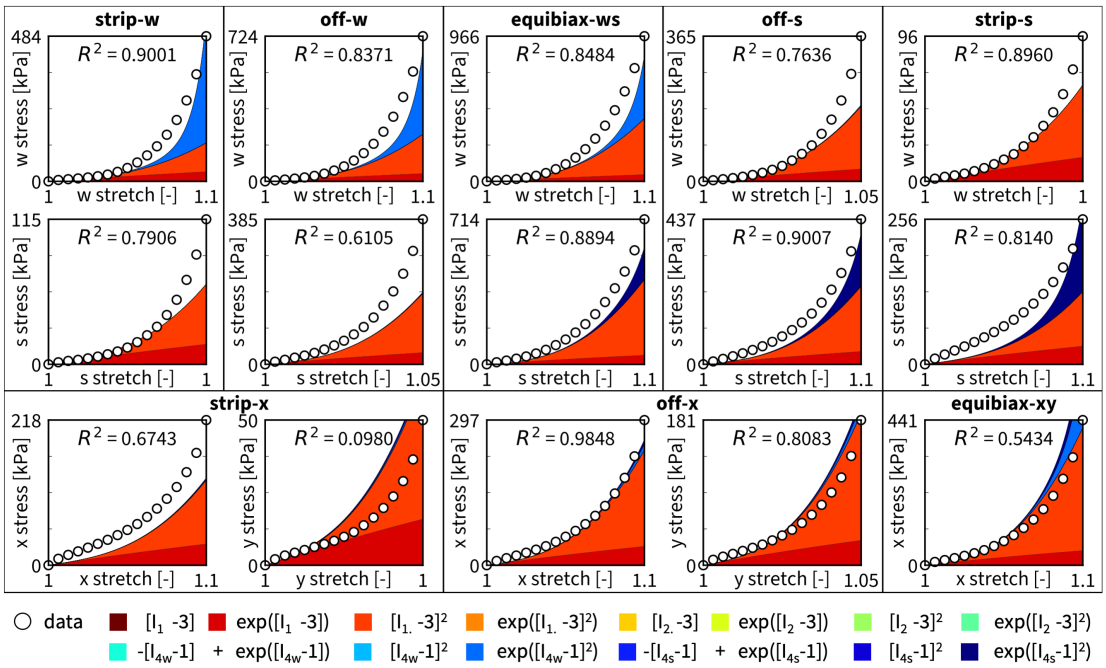

Figure 7: **Discovered two-fiber model and biaxial test data.** We train the two-fiber constitutive neural network from Figure 3 on all 15 data sets and sparsify the discovered model with $L_{0.5}$ regularization. The network discovers a four-term model with two isotropic terms and two anisotropic terms, which we plot in their characteristic colors. The R^2 values suggest that the discovered model performs decent on most of the tests in the 0/90 orientation, but performs particularly poorly on the strip-x experiment in the -45/+45 orientation where it underpredicts the x-stress and overpredicts the y-stress. The mean R^2 value across all tests is 0.7573.

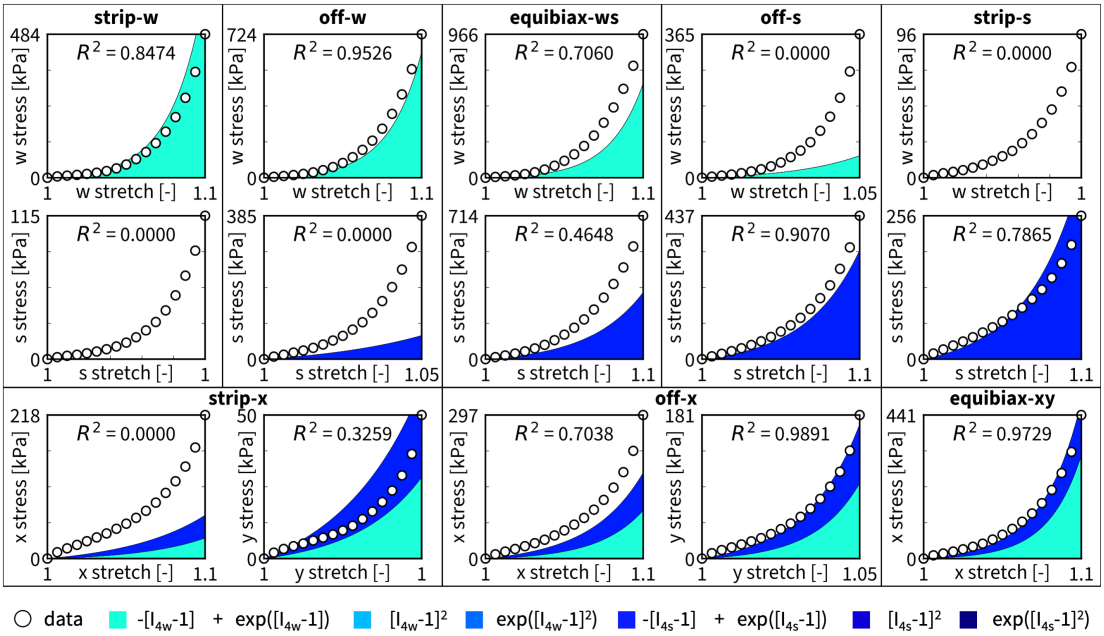

Figure 8: **Discovered anisotropic two-fiber model and biaxial test data.** We train the two-fiber constitutive neural network from Figure 4 on all 15 data sets and constrain the weights for the isotropic terms to be zero. The network discovers a two-term model with one term that is a function of the fourth warp invariant I_{4w} and one that is a function of the fourth shute invariant I_{4s}, which we plot in their characteristic colors. The R^2 values suggest that the discovered model performs poorly on most tests, with R^2 values of zero for several tests. The mean R^2 value across all tests is 0.5104.

two-term models by sampling all 14 single terms and all 91 pairs of two terms. Figure 12 shows the minimized loss for all 105 combination of terms. The first eleven terms in the three-fiber architecture are identical to the first eleven terms in the two-fiber architecture, which means the only difference between Figures 9 and 12 are the last three rows and columns associated with the shute invariants I_{4s_I} and $I_{4s_{II}}$. Interestingly, for the three-fiber architecture, the best-in-class two-term model is identical to the discovered non-isotropic model with two exponential linear Weiss terms [51], one in the fourth warp invariant

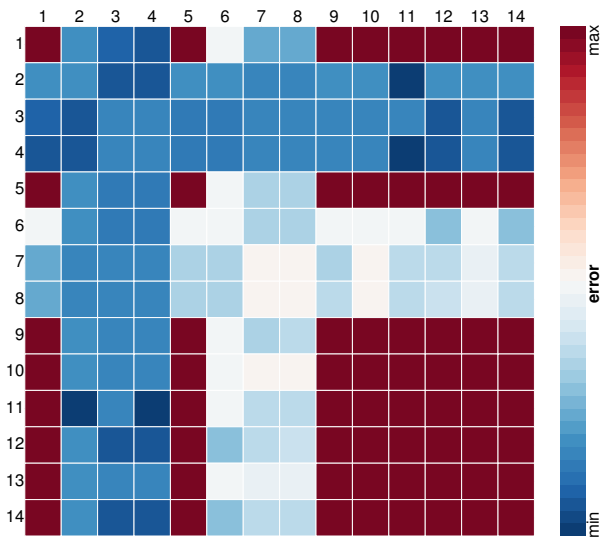

Figure 9: **Best-in-class one- and two-term two-fiber models.** All models are made up of 14 functional building blocks: linear, exponential linear, quadratic, and exponential quadratic terms of the first invariant I_1, rows and columns 1 to 4, of the second invariant I_2, rows and columns 5 to 8, of the fourth warp invariant I_{4w} rows and columns 9 to 11, and of the fourth shute invariant I_{4s} rows and columns 12 to 14. The color code indicates the mean squared error of the 14 one-term models on the diagonale, and of the 91 two-term models on the off-diagonale, ranging from dark blue, best fit, to dark red, worst fit.

I_{4w} and one in the fourth shute invariants I_{4s_I} and $I_{4s_{II}}$,

$$\psi = \tfrac{1}{2}a_1\,[\exp(b_1[I_{4w} \;\; -1]) - 1]/b_1 - \tfrac{1}{2}a_1\,[I_{4w} - 1] \\ + \tfrac{1}{2}a_2\,[\exp(b_2(I_{4s_{I,II}} - 1]) - 1]/b_2 - \tfrac{1}{2}a_2\,]I_{4s_{I,II}} - 1]$$

with the two stiffness-like parameters, $a_1 = 1.26\,\text{kPa}$, $a_2 = 28.93\,\text{kPa}$, and the two nonlinearity parameters $b_1 = 24.55$, $b_2 = 7.20$, and a training loss of 0.04. Strikingly, of all possible one- and two-term models, the best model characterizes the warp knitted mesh without any isotropic terms, and is exclusively made up of exponential linear terms of the squared stretches along the microstructural directions of the mesh.

3.4. Training and testing

To demonstrate that our discovered models have predictive capability beyond the data used in training, we train the network using a subset of the data and use the remaining data to test model performance. Yet, rather than randomly partitioning the available data into a training and test sets, we choose each of the tests to either be entirely part of the training set or test set. This is because the observations within a single test are highly correlated, and a constitutive model is most useful if it is capable of accurately predicting the resulting stress when the applied deformation takes a form that differs from the training data. We train the network with the three-fiber architecture from Figure 4 using four different training sets: the first training set consists of all experiments, the second consists of only experiments in the 0/90 orientation; the third consists of only experiments in the +45/-45 orientation; and the fourth consists of all experiments except strip-shute loading in the 0/90 orientation. Figure 13 shows the resulting coefficient of determination R^2 for each stress-stretch curve when training the model on each of these four training sets. The figure illustrates that it is insufficient to train exclusively on the tests in the 0/90 orientation or on tests in the +45/-45 orientation; data from both orientations are essential to fully understand the constitutive behavior of our mesh. Notably, the model performance on the strip-shute tests when trained with all data except strip-shute is remarkably similar to the model performance when trained on all data. This suggests that the model is capable of extrapolating to unseen data, and shows that it does not overfit the training data.

4. Discussion

Synthetic meshes have unique mechanical properties, which make them ideal candidates for many engineering and medical applications. *The objective of this study was to provide insights into the mechanical signature of synthetic meshes using an integrative approach that combines biaxial testing and automated model discovery.* We prototyped this approach using a 0.5 mm thick warp knitted surgical mesh of extruded polypropylene. We tested the mesh in two different orientations, the 0/90 orientation with the loading axis aligned with the warp direction, and the -45/+45 orientation with the loading axis inclined by 45 degrees to the warp direction. We compared two families of microstructural models, a two-fiber model with a warp direction $\boldsymbol{w}$ and one orthogonal shute direction $\boldsymbol{s}$, and a three-fiber model with a warp direction $\boldsymbol{w}$ and two symmetrical shute directions $\boldsymbol{s}_I$ and $\boldsymbol{s}_{II}$ inclined by 60 degrees. Our study confirms our intuition that knitted meshes display a remarkable *initial flexibility*, a pronounced *nonlinear stiffening*, and an *extreme anisotropy*. Beyond these expected observations, it also reveals several exciting features of polypropylene meshes.

Exponential linear fourth invariant terms dominate the constitutive response of polypropylene meshes. Throughout this study, we pursued different approaches to discover the best model and parameters to characterize textile structures. We trained a full neural network with fourteen independent terms and a subset of the network with only the six anisotropic terms, both for the two- and three-fiber model, with pronounced directions inclined by either 90 or 60 degrees. This allows us to discover the best model and parameters out of $2^{14} = 16,384$ and $2^6 = 64$ possible combinations of terms. Strikingly, one term reoccured consistently through automated model discovery: the exponential linear fourth invariant term, $\frac{1}{2}\,a\,[\exp(b\,[I_4 - 1]) - 1]/b - \frac{1}{2}\,a\,[I_4 - 1]$. Originally proposed for soft biological tissues [51], this term is ideally suited to characterize the remarkable *initial flexibility* of the virgin mesh and the pronounced *nonlinear stiffening* as the loops of the mesh tighten upon loading. Of all four discovered models in Figures 7, 8, 10, and 11, three prominently feature this exponential linear fourth invariant term, both in the warp and shute directions I_{4w} and I_{4s}, highlighted through the turquoise and blue colors. We confirm the dominance of these two terms with an entirely independent best-in-class modeling study in Figures 9 and 12 that also identifies the the turquoise and blue terms to make up the best-in-class two-term model out of 91 possible two-term

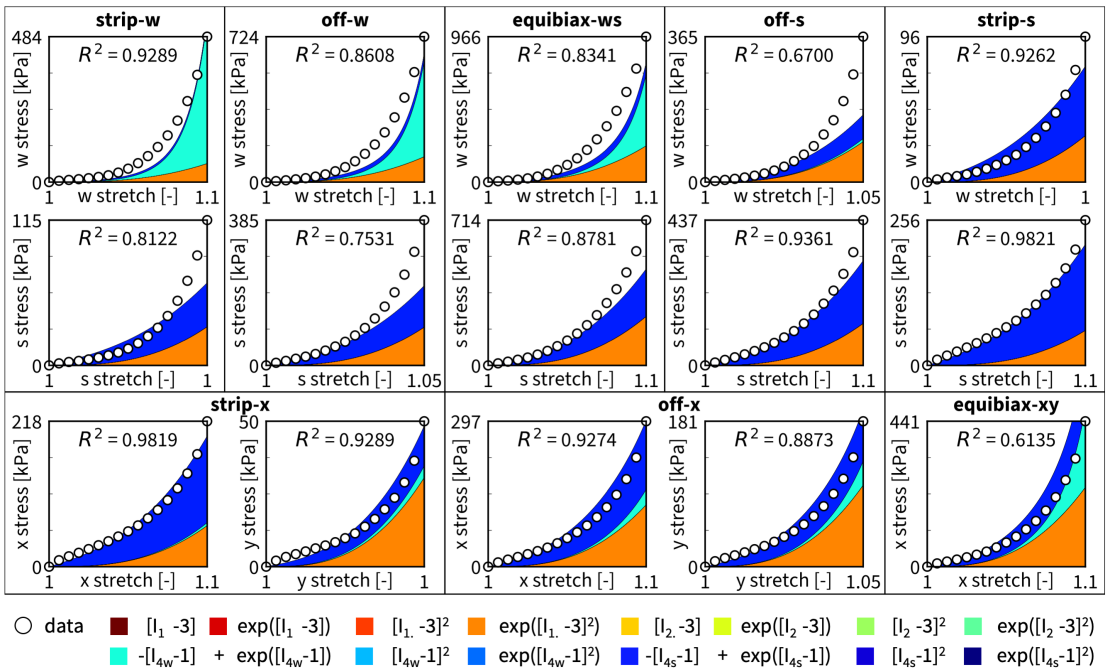

Figure 10: **Discovered three-fiber model and biaxial test data.** We train the three-fiber constitutive neural network from Figure 4 on all 15 data sets and sparsify the discovered model with $L_{0.5}$ regularization. The network discovers a three-term model with one isotropic term and two anisotropic terms, which we plot in their characteristic colors. The R^2 values suggest that the discovered model performs well on all fifteen tests. The mean R^2 value across all tests is 0.8614.

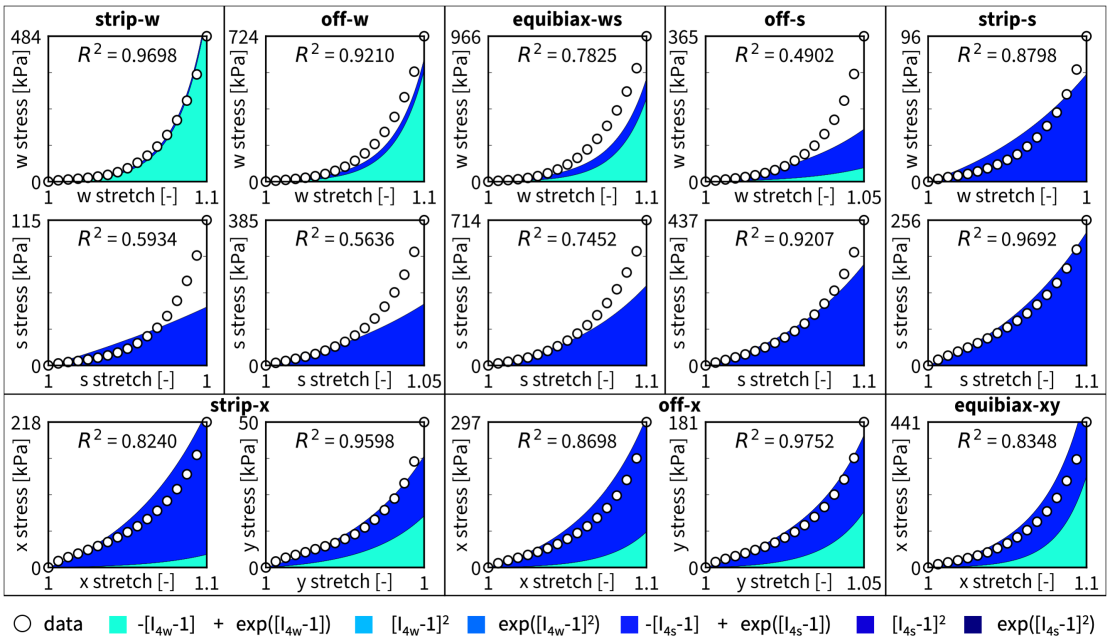

Figure 11: **Discovered anisotropic three-fiber model and biaxial test data.** We train the three-fiber constitutive neural network from Figure 4 on all 15 data sets and constrain the weights for the isotropic terms to be zero. The network discovers a two-term model with one term that is a function of the fourth warp invariant I_{4w} and one that is a function of the fourth shute invariants I_{4s_I} and $I_{4s_{II}}$, which we plot in their characteristic colors. The model that is discovered is very similar to the optimal two-term model shown in figure 12. The R^2 values suggest that, even without isotropic terms, the discovered model performs well across all fifteen tests. The mean R^2 value across all tests is 0.8199.

models, both for the two- and three-fiber microstructure. Interestingly, the full network model in Figure 10 with a mean R^2 value of 0.8614 performs only marginally better than the reduced network model in Figure 11 with a mean R^2 value of 0.8199. This suggest that we can confidently use the discovered two-term fourth-invariant model that features no isotropic terms to characterize the *ultra-anisotropic* nature of polypropylene meshes.

Mixed invariant terms are critical to characterize the in-

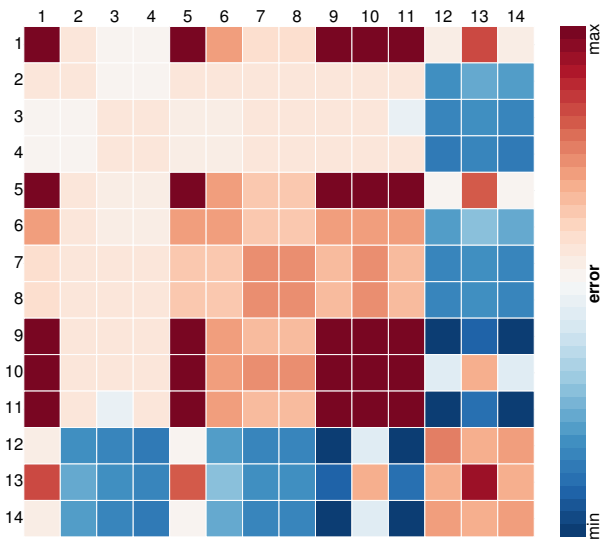

Figure 12: **Best-in-class one- and two-term three-fiber models.** All models are made up of 14 functional building blocks: linear, exponential linear, quadratic, and exponential quadratic terms of the first invariant I_1, rows and columns 1 to 4, of the second invariant I_2, rows and columns 5 to 8, of the fourth warp invariant I_{4w} rows and columns 9 to 11, and of the fourth shute invariants I_{4s_I} and $I_{4s_{II}}$ rows and columns 12 to 14. The color code indicates the mean squared error of the 14 one-term models on the diagonale, and of the 91 two-term models on the off-diagonale, ranging from dark blue, best fit, to dark red, worst fit.

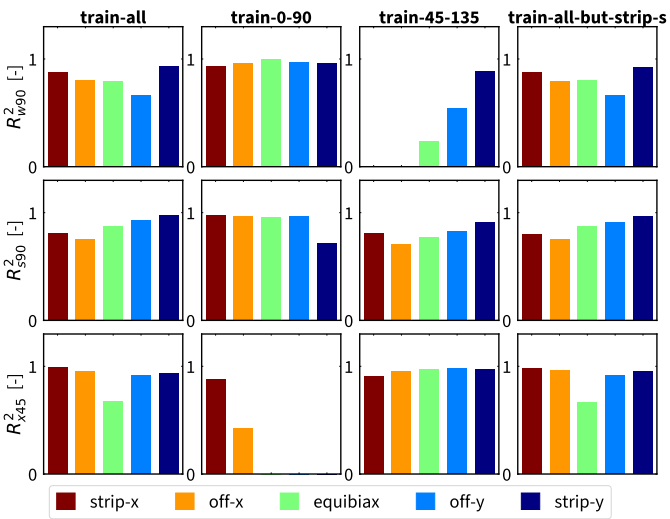

Figure 13: **Performance of three-fiber network for four different training sets.** The columns represent the four training sets: data from only the 0/90 orientation, data from only the +45/-45 orientation, all data, and all data except the strip-s data in the 0/90 orientation. The rows represent the coefficients of determination of the warp stress in the 0/90 orientation, the shute stress in the 0/90 orientation, and the x stress in the +45/-45 orientation. To accurately predict the stress in all loading conditions, the training set must include data from both the 0/90 and +45/-45 orientations.

teraction of the warp and shute directions. To systematically explore the importance of the mixed invariant I_{8ws}, we studied two different microstructural models. Figure 2 illustrates their two distinct microstructures, which represent the loops of the mesh as through warp direction $\boldsymbol{w}$ and the underlap through a single orthogonal shute direction $\boldsymbol{s}$ or two shoot directions $\boldsymbol{s}_I$ and $\boldsymbol{s}_{II}$, symmetrically offset by 60 degrees [15]. A direct comparison of the performance of our discovered two-fiber and three-fiber models in Figures 7 and 10 suggests that incorporating detailed microstructural information along all three directions is critical for model accuracy [45]. In Figure 7, we can see that the two-fiber model significantly under-predicts the x-stress and over-predicts the y-stress for the strip-x experiment in the +45/-45 orientation, To show that this error is a direct consequence of the two-fiber model, we take a closer look at the anisotropic stress contributions. In particular, when the strain energy is not a function of I_{8ws}, the contribution of the anisotropic terms to the x- and y-stress in the +45/-45 orientation is $P^{\text{ani}}_{xx} = \lambda_x(\partial\psi/\partial I_{4w} + \partial\psi/\partial I_{4s})$ and $P^{\text{ani}}_{yy} = \lambda_y(\partial\psi/\partial I_{4w} + \partial\psi/\partial I_{4s})$, thus, $P^{\text{ani}}_{xx}/P^{\text{ani}}_{yy} = \lambda_x/\lambda_y$. At maximum strip-x loading in the +45/-45 orientation, the stretches are $\lambda_x = 1.1$ and $\lambda_y = 1.0$, such that $\lambda_x/\lambda_y = 1.1$, and the stresses are $P^{\text{ani}}_{xx} = 219\,\text{kPa}$ and $P^{\text{ani}}_{yy} = 50\,\text{kPa}$, such that $P^{\text{ani}}_{xx}/P^{\text{ani}}_{yy} = 4.38$. We can directly see this discrepancy in Figure 8, where the discovered model has an R^2 value of zero for the x-stress in strip-x loading in the +45/-45 orientation. This suggests that an appropriate model for warp knitted meshes should indeed be a function of the mixed invariant I_{8ws}. If the strain energy ψ is a function of the mixed invariant I_{8ws} [27], the derivative $\partial\psi/\partial I_{8ws}$ contributes a positive component to P^{ani}_{xx} and a negative component to P^{ani}_{yy}. For positive mixed invariants, $\partial\psi/\partial I_{8ws} > 0$, such that $P^{\text{ani}}_{xx} \geq P^{\text{ani}}_{yy}$, and thus $P^{\text{ani}}_{xx}/P^{\text{ani}}_{yy} \geq \lambda_x/\lambda_y$, which is what we observe in Table 2. This observation is in line with several previous studies that have acknowledged the importance of the mixed invariant for double-fiber reinforced nonlinear elastic materials [29].

Understanding the shear response is critical to model textile structures. Even with an appropriate constitutive neural network that is informed by the microstructure of the mesh, our inability to measure shear strain in biaxial loading [7] results in a loss of model accuracy in certain loading modes. Most obviously, when comparing Figures 7 and 10, we notice that the model generally under-predicts the shute and warp stresses in the 0/90 orientation, and over-predicts the x- and y-stresses in the +45/-45 orientation. When taking a closer look at the states of maximum deformation in equibiaxial loading, we see that when $\lambda_w = \lambda_s = \lambda = 1.1$ in the 0/90 orientation, the invariants and mixed invariants are identical to when $\lambda_x = \lambda_y = \lambda = 1.1$ in the +45/-45 orientation. In both cases, $I_1 = 2\lambda^2 + \lambda^{-4}$ and $I_2 = 2\lambda^{-2} + \lambda^4$ and $I_{4w} = I_{4s} = \lambda^2$ and $I_{8ws} = 0$. As a result, the strain energy ψ and its partial derivatives are identical in both cases. Thus, $P^{\text{ani}}_{ww} = 2\lambda\,\partial\psi/\partial I_{4w}$ and $P^{\text{ani}}_{ss} = 2\lambda\,\partial\psi/\partial I_{4s}$ and $P^{\text{ani}}_{xx} = \lambda\,(\partial\psi/\partial I_{4w} + \partial\psi/\partial I_{4s} + \partial\psi/\partial I_{8ws})$. Since $I_{8ws} = 0$ and ψ is an even function of I_{8ws}, by symmetry, we know that $\partial\psi/\partial I_{8ws} = 0$, and thus, $P_{ww} + P_{ss} = 2\,P_{xx}$. However, looking at the data, $P_{ww} + P_{ss} = 996$ kPa + 714 kPa = 1710 kPa, while $2\,P_{xx} = 884$ kPa. This contradiction is triggered by our assumptions in equations (5) and (16) that the deformation remains homogeneous and shear free at all times, such that the deformation gradient $\boldsymbol{F}$ remains diagonal, $\boldsymbol{F} = \text{diag}\{\lambda_x, \lambda_y, \lambda_x^{-1}\lambda_y^{-1}\}$. This condition holds for sam-

ples loaded in biaxial tension, if their microstructure is symmetric about the two loading directions. While this is true for isotropic materials in general, and it holds for orthotropic materials in the 0/90 configuration, it does not hold for orthotropic materials in the +45/-45 configuration: Loading non-symmetrically mounted orthotropic materials in biaxial tension tests may actually result in non-zero shear strains [41]. Since the CellScale BioTester 5000 grips the material using slender tines that are stiff in tension but compliant in bending, a more accurate boundary condition would be that the axial stretches are equal to the values measured by the device, and the shear stresses are equal to zero. In this case, the shear strains would be non-zero and would take the values that minimize the strain energy given the prescribed axial stretches in the two loading direcions. This change would decrease the predicted strain energy in the +45/-45 orientation, while leaving the strain energy in the 0/90 orientation unchanged. As a result, we would expect $2P_{xx} < P_{ww} + P_{ss}$, which is indeed what we observe in Table 2. To accurately incorporate this effect, we would need to measure the shear strain, which the CellScale BioTester 5000 does not directly control or measure. A possible future direction would be to quantify shear strain using full field data from digital image correlation.

Our networks reliably extrapolate to unseen data. Our study confirms, that with an appropriate microstructural representation, our constitutive neural network discovers generalizable anisotropic constitutive models, provided that we use training data from both the 0/90 and +45/-45 orientations. From the goodness-of-fit bar plots in Figure 13, it is clear that training on only data from the 0/90 orientation results in inaccurate model predictions in the +45/-45 orientation, and vice versa. This result is not surprising since certain characteristics of the material are only active and visible in one of the two orientations. In particular, in the +45/-45 orientation, by symmetry $I_{4w} = I_{4s}$ for all loading states, which means that it is not possible to independently probe the I_{4w} and I_{4s} terms. Similarly, in the 0/90 orientation, $I_{8ws} = 0$ for all loading states of the two-fiber models, so we cannot measure the effect of I_{8ws} on the stress. Thus, the training data must consist of data from both orientations for the model to robustly predict stresses under all possible conditions. Another interesting observation from Figure 13 is that, when training on all the available data except the strip-shute data in the 0/90 configuration, the discovered model achieves similar R^2 values for the training and test data when compared to the model trained on all the data. This suggests that our model is not overfitting the data, and that when trained on a subset of data from both orientations, it is able to accurately predict the stresses for deformation states that we do not use in training.

5. Conclusion

Characterizing the mechanical properties of synthetic meshes is critical to understand their unique properties and functions. To date, identifying appropriate constitutive models for woven and knitted textiles poses a critical barrier to mechanically tailoring and fine-tuning these structures to individual needs. Machine-learning approaches can discover anisotropic constitutive models from biaxial data; yet, existing approaches are limited to training data from a single mounting orientation. Here we show that this approach can result in superficial constitutive models that generalize poorly to unseen data. In contrast, the new approach we advocate here uses data from at least two different mounting orientations, and robustly discovers models that perform well during both training and testing. Importantly, our study shows that the accuracy of the discovered models is highly sensitive to an accurate representation of the microstructural architecture of the sample: Even if the textile fabric appears orthotropic at first glance, an accurate kinematic characterization of both warp and shute directions is critical to discover robust and reliable models. We demonstrate that these models are dominated by exponential linear fourth invariant terms that uniquely capture the remarkable initial flexibility, pronounced nonlinear stiffening, and extreme anisotropy of warp knitted polypropylene meshes. We anticipate that the tools we have developed here will generalize naturally to other textile fabrics–woven or knitted, weft knit or warp knit, with laid-in stitches or plain, polymeric or metallic–and, ultimately, will enable the robust discovery of anisotropic constitutive models for a wide variety of textile structures. Beyond discovering constitutive models, we envision to exploit automated model discovery as a novel strategy for the generative material design of wearable devices, stretchable electronics, and smart fabrics, as programmable textile metamaterials with tunable properties and functions.

Data availability

Our source code, data, and examples are available at https://github.com/LivingMatterLab/CANN.

Acknowledgments

This work was supported by the NSF Graduate Student Fellowship to Jeremy A. McCulloch and by the NSF CMMI Award 2320933 Automated Model Discovery for Soft Matter and by the ERC Advanced Grant 101141626 DISCOVER to Ellen Kuhl.

References

[1] K. Baylon, P. Rodriguez-Camarillo, A. Elias-Zuniga, J.A. Diaz-Elizondo, R. Gilkerson, K. Lozano. Past, present and future of surgical meshes: A review. *Membranes* 7:47, 2017.

[2] I. Bettermann, H. Löcken, C. Greb, T. Gries, A. Oses, J. Pauw, N. Maghaldadze, L. Datashvili. Review and evaluation of warp-knitted patterns for metal-based large deployable reflector surfaces. em CEAS Space Journal 15:477–493, 2023.

[3] S.L. Brunton, P.J. Proctor, and J.N. Kutz. Discovering governing equations from data by sparse identification of nonlinear dynamical systems. *Proceedings of the National Academy of Sciences*, 113:3932–3937, 2016.

[4] E.B. Deerenberg, J.Verhelst, S.E.R. Hovius, and J.F. Lange. Mesh expansion as the cause of bulging after abdominal wall hernia repair. *International Journal of Surgery Case Reports*, ' 28:200–203, 2016.

[5] H. Demiray. A note on the elasticity of soft biological tissues. *Journal of Biomechanics*, 5:309–311, 1972.

[6] S. Est, M. Roen, T. Chi, A. Simien, R.M. Castile, D.M. Thompson, J.A. Blatnik, C.R. Deeken, S.P. Lake. Multi-directional mechanical analysis of synthetic scaffolds for hernia repair. *Journal of the Mechanical Behavior of Biomedical Materials*, 71:43–53, 2017.

[7] H. Fehervary, Ma. Smoljkic, J. Vander Sloten, N. Famaey. Planar biaxial testing of soft biological tissue using rakes: A critical analysis of protocol and fitting process *Journal of the Mechanical Behavior of Biomedical Materials* 61: 135-151, 2016.

[8] J.N. Fuhg, R.E. Jones, N. Bouklas. Extreme sparsification of physics-augmented neural networks for interpretable model discovery in mechanics. *Computer Methods in Applied Mechanics and Engineering*, 426:116973, 2024.

[9] W. He, G. Cao, X. Gan, Y. Fan, B. Pei, X. Li. Evaluation methods for mechanical biocompatibility of hernia repair meshes: respective characteristics, application scope and future perspectives. *Journal of Materials Research and Technology*, 13:1826–1840, 2021.

[10] Hastie T, Tibshirani R, Friedman J. The Elements of Statistical Learning. Second Edition; 2009. Springer, New York.

[11] G.A. Holzapfel, T.C. Gasser, R.W. Ogden. A new constitutive framework for arterial wall mechanics and comparative study of material models. *Journal of Elasticity*, 61:1–48, 2000.

[12] G.A. Holzapfel. Nonlinear Solid Mechanics: A Continuum Approach to Engineering. 2000. John Wiley & Sons, Chichester.

[13] J. Hu, B. Kumar, J. Lu. Handbood of Fibrous Materials. Wiley-VCH Verlag, Weinheim, Germany, 2000.

[14] C. Jiang, K. Wang, Y. Liu, C. Zhang, B. Wang. Application of textile technology in tissue engineering: A review *Acta Biomaterialia*, 128:60–76, 2021.

[15] Y. Kyosev. Topology-Based Modeling of Textile Structures and their Joint Assemblies. Principles, Algorithms and Limitations. Springer Nature Switzerland, 2019.

[16] Y.Lanir and Y.C. Fung. Two-dimensional mechanical properties of rabbit skin—II. Experimental results. *Journal of Biomechanics*, 7:171–182, 1974.

[17] A. Liberski, N. Ayad, D. Wojciechowska, D. Zieliska, M.H. Struszczyk, N. Latif, M. Yacoub. Knitting for heart valve tissue engineering. *Global Cardiology Science and Practice*, 31:1-33, 2016.

[18] K.Linka, M.Hillgartner, K.P. Abdolazizi, R.C. Aydin, M.Itskov, C.J. Cyron. Constitutive artificial neural networks: A fast and general approach to predictive data-driven constitutive modeling by deep learning. *Journal of Computational Physics*, 429:110010, 2021.

[19] K. Linka, E. Kuhl. A new family of Constitutive Artificial Neural Networks towards automated model discovery. *Computer Methods in Applied Mechanics and Engineering*, 403:115731, 2023.

[20] K. Linka, S.R. St Pierre, E. Kuhl. Automated model discovery for human brain using Constitutive Artificial Neural Networks. *Acta Biomaterialia* 160:134-151, 2023.

[21] K. Linka, A. Buganza Tepole, G.A. Holzapfel, E. Kuhl. Automated model discovery for skin: Discovering the best model, data, and experiment. *Computer Methods in Applied Mechanics and Engineering*, 410:116007, 2023.

[22] L. Liu, P. Ma. Review on the performances and applications of mesh-fabrics. *Journal of Industrial Textiles*, 52: 1–28, 2022.

[23] D. Martonova, M. Peirlinck, K. Linka, G.A. Holzapfel, S. Leyendecker, E. Kuhl. Automated model discovery for human cardiac tissue: Discovering the best model and parameters. *Computer Methods in Applied Mechanics and Engineering*, 428:117078, 2024.

[24] M.M. Maurer, B. Röhrnbauer, A. Feola, J. Deprest, E. Mazza. Mechanical biocompatibility of prosthetic meshes: A comprehensive protocol for mechanical characterization. *Journal of the Mechanical Behavior of Biomedical Materials*, 40: 42-58, 2014.

[25] J.A. McCulloch, S.R. St.Pierre, K. Linka, E. Kuhl. On sparse regression, Lp-regularization, and automated model discovery. *International Journal for Numerical Methods in Engineering*, 125:e7481, 2024.

[26] W.D. Meador, G.P. Sugerman, A. Buganza Tepole, M.K. Rausch. Biaxial mechanics of thermally denaturing skin. *Acta Biomaterialia*, 140:412-420, 2022.

[27] A.V. Melnik, X. Luo, R.W. Ogden. A generalised structure tensor model for the mixed invariant I8. *International Journal of Non-Linear Mechanics*, 107:137–148, 2018.

[28] A. Menzel. Frontiers in Inelastic Continuum Mechanics. Habilitation Thesis. Technical University of Kaiserslautern, 2007.

[29] J. Merodio, R.W. Ogden. The influence of the invariant I8 on the stress–deformation and ellipticity characteristics of doubly fiber-reinforced non-linearly elastic solids. *International Journal of Non-Linear Mechanics*, 41:556–563, 2006.

[30] I.H. Mondal, M. Islam, I. Haque, F. Ahmed. Natural, biodegradable, biocompatible and bioresorbable medical textile materials. In: *Medical Textiles from Natural Resources*, 87-116, 2023.

[31] A. Morch. L. Astruc, J.F. Witz, F. Lesaffre, P. Lecompte-Grosbras, D. Soulat, M. Brieu. Modeling of anisotropic hyperelastic heterogeneous knitted fabric reinforced composites. *Journal of the Mechanics and Physics of Solids*, 127:47-61, 2019.

[32] J.L. Ng, C.E. Collins, M.L. Knothe Tate. Engineering mechanical gradients in next generation biomaterials – Lessons learned from medical textile design. *Acta Biomaterialia*, 56: 14-24, 2017.

[33] S.W. Nienhuijs, C.Rosman, L.J.A. Strobbe, A.Wolff, R.P. Bleichrodt. An overview of the features influencing pain after inguinal hernia repair. *International Journal of Surgery*, 6:351–356, 2008.

[34] E.M. Parsons, T. Weerasooriya, S. Sarva, S. Socrate. Impact of woven fabric: Experiments and mesostructure-based continuum-level simulations *Journal of the Mechanics and Physics of Solids*, 58: 1995-2021, 2010.

[35] M.Peirlinck, K.Linka, J.A. Hurtado, G.A. Holzapfel, E.Kuhl. Democratizing biomedical simulation through automated model discoveryand a universal material subroutine. *Computational Mechanics; in press*, doi:10.1101/2023.12.06.570487, 2024.

[36] S.R. St Pierre, K.Linka, and E.Kuhl. Principal-stretch-based constitutive neural networks autonomously discover a subclass of Ogden models for human brain tissue. *Brain Multiphysics*, 4:100066, 2023.

[37] S.R. St Pierre, D. Rajasekharan, E.C. Darwin, K. Linka, M.E. Levenston, E. Kuhl. Discovering the mechanics of artificial and real meat. *Computer Methods in Applied Mechanics and Engineering* 415:116236, 2023.

[38] M.Raissi, P.Perdikaris, G.E. Karniadakis. Physics-informed neural networks: a deep learning framework for solving forward and inverse problems involving nonlinear partial differential equations. *Journal of Computational Physics*, 378:686–707, 2019.

[39] W. Renkens, Y. Kyosev. Geometry modelling of warp knitted fabrics with 3D form *Textile Research Journal*, 81: 437–443, 2010.

[40] B. Röhrnbauer, Y. Ozog, J. Eggerc, E. Werbrouck, J. Deprest, E. Mazza. Combined biaxial and uniaxial mechanical characterization of prosthetic meshes in a rabbit model. *Journal of Biomechanics*, 46: 1626-1632, 2013.

[41] B. Röhrnbauer, E. Mazza. Uniaxial and biaxial mechanical characterization of a prosthetic mesh at different length scales. *Journal of the Mechanical Behavior of Biomedical Materials*, 29: 7-19, 2014.

[42] M.P. Simons, M.Smietanski, H.J. Bonjer, R.Bittner, M.Miserez, Th.J. Aufenacker, R.J. Fitzgibbons, P.K. Chowbey, H.M. Tran, R.Sani, F.Berrevoet, J.Bingener, T.Bisgaard, K.Bury, G.Campanelli, D.C. Chen, J.Conze, D.Cuccurullo, A.C. deBeaux, H.H. Eker, R.H. Fortelny, J.F. Gillion, B.J. vanden Heuvel, W.W. Hope, L.N. Jorgensen, U.Klinge, F.Köckerling, J.F. Kukleta, I.Konate, A.L. Liem, D.Lomanto, M.J.A. Loos, M.Lopez-Cano, M.C. Misra, A.Montgomery, S.Morales-Conde, F.E. Muysoms, H.Niebuhr, P.Nordin, M.Pawlak, G.H. van Ramshorst, W.M.J. Reinpold, D.L. Sanders, N.Schouten, S.Smedberg, R.K.J. Simmermacher, S.Tumtavitikul, N.van Veenendaal, D.Weyhe, A.R. Wijsmuller, and The HerniaSurge Group. International guidelines for groin hernia management. *Hernia*, 22:1–165, 2018.

[43] K. Singal, M.S. Dimitriyev, S.E. Gonzalez, A.P. Cachine1, S. Quinn, E.A. Matsumoto. Programming mechanics in knitted materials, stitch by stitch. *Nature Communications*, 15:2622, 2024.

[44] A.J.M. Spencer. Theory of Invariants. In: Eringen AC, Ed., Continuum Physics Vol. 1: 239-353, Academic Press, New York, 1971.

[45] A.J.M. Spencer. A theory of viscoplasticity for fabric-reinforced composites. *Journal of the Mechanics and Physics of Solids*, 49:2667-2687, 2001.

[46] V. Tac, V.D. Sree, M.K. Rausch, A. Buganza Tepole. Data-driven modeling of the mechanical behavior of anisotropic soft biological tissues. *Engineering with Computers*, 38:4167-4182, 2022.

[47] V. Tac, K. Linka, F. Sahli Costabal, E. Kuhl, A. Buganza Tepole. Benchmarking physics-informed frameworks for data-driven hyperelasticity. *Computational Mechanics* 73:49-65, 2024.

[48] L.R.G. Treloar. Stresses and birefringence in rubber subjected to general homogeneous strain. *Proceedings of the Physical Society*, 63:135–144, 1948.

[49] K. Vander Linden, H. Fehervary, L. Maes, N. Famaey. An improved parameter fitting approach of a planar biaxial test including the experimental prestretch. *Journal of the Mechanical Behavior of Biomedical Materials*, 134: 105389, 2022.

[50] C. W. See, T. Kim, D. Zhu. Hernia mesh and hernia repair: A review. *Engineered Regeneration*, 1:19–33, 2020.

[51] J.A. Weiss, B.N. Marker, S.Govindjee. Finite element implementation of incompressible, transversely isotropic hyperelasticity. *Computer Methods in Applied Mechanics and Engineering*, 135:107–128, 1996.